Remote Sensing of Environment 222 (2019) 1–17

Contents lists available at ScienceDirect

Remote Sensing of Environment

journal homepage: www.elsevier.com/locate/rse

Development of a Sentinel-2 burned area algorithm: Generation of a small fire database for sub-Saharan Africa

E. Roteta[a,*], A. Bastarrika[a], M. Padilla[b], T. Storm[c], E. Chuvieco[d]

[a] Department of Mining and Metallurgical Engineering and Materials Science, School of Engineering of Vitoria-Gasteiz, University of the Basque Country UPV/EHU, Nieves Cano 12, 01006 Vitoria-Gasteiz, Spain
[b] Centre for Landscape and Climate Research, Department of Geography, University of Leicester, Leicester, United Kingdom
[c] Brockmann Consult GmbH, Max-Planck-Straße 2, 21502 Geesthacht, Germany
[d] Environmental Remote Sensing Research Group, Department of Geology, Geography and the Environment, University of Alcalá, C/Colegios 2, 28801 Alcalá de Henares, Spain

ARTICLE INFO

Keywords:
Sentinel-2
MSI
Burned Area Mapping
Africa
Fires

ABSTRACT

A locally-adapted multitemporal two-phase burned area (BA) algorithm has been developed using as inputs Sentinel-2 MSI reflectance measurements in the short and near infrared wavebands plus the active fires detected by Terra and Aqua MODIS sensors. An initial burned area map is created in the first step, from which tile dependent statistics are extracted for the second step. The whole Sub-Saharan Africa (around 25 M km^2) was processed with this algorithm at a spatial resolution of 20 m, from January to December 2016. This period covers two half fire seasons on the Northern Hemisphere and an entire fire season in the South. The area was selected as existing BA products account it to include around 70% of global BA. Validation of this product was based on a two-stage stratified random sampling of Landsat multitemporal images. Higher accuracy values than existing global BA products were observed, with Dice coefficient of 77% and omission and commission errors of 26.5% and 19.3% respectively. The standard NASA BA product (MCD64A1 c6) showed a similar commission error (20.4%), but much higher omission errors (59.6%), with a lower Dice coefficient (53.6%). The BA algorithm was processed over > 11,000 Sentinel-2 images to create a database that would also include small fires (< 100 ha). This is the first time a continental BA product is generated from medium resolution sensors (spatial resolution = 20 m), showing their operational potential for improving our current understanding of global fire impacts. Total BA estimated from our product was 4.9 M km^2, around 80% larger area than what the NASA BA product (MCD64A1 c6) detected in the same period (2.7 M km^2). The main differences between the two products were found in regions where small fires (< 100 ha) account for a significant proportion of total BA, as global products based on coarse pixel sizes (500 m for MCD64A1) unlikely detect them. On the negative side, Sentinel-2 based products have lower temporal resolution and consequently are more affected by cloud/cloud shadows and have less temporal reporting accuracy than global BA products. The product derived from S2 imagery would greatly contribute to better understanding the impacts of small fires in global fire regimes, particularly in tropical regions, where such fires are frequent. This product is named FireCCISFD11 and it is publicly available at: https://www.esa-fire-cci.org/node/262, last accessed on November 2018.

1. Introduction

Biomass burning is a key element of the terrestrial carbon cycle and a significant source of atmospheric trace gases and aerosols (Andreae and Metlet, 2001). Depending on their size, location and timing, fires significantly modify land surface properties, influence atmospheric chemistry and air quality, through aerosol and gas emissions, while modifying albedo by land use transformations (Bowman et al., 2009).

Satellite Earth observation is extensively used to detect burned areas (BA) and active fires. BA detection is commonly based on the effects of fire on vegetation reflectance, while the detection of active fires is mainly based on the thermal contrast between burnings and the background (Giglio et al., 2016; Schroeder et al., 2016, 2014). In recent years, several global burned area (BA) products have been made available to the international community. The first released were the Global Burned Area 2000-GBA2000 (Tansey et al., 2004), and

* Corresponding author.
E-mail address: ekhi.roteta@ehu.eus (E. Roteta).

https://doi.org/10.1016/j.rse.2018.12.011
Received 29 September 2017; Received in revised form 18 November 2018; Accepted 8 December 2018
Available online 20 December 2018

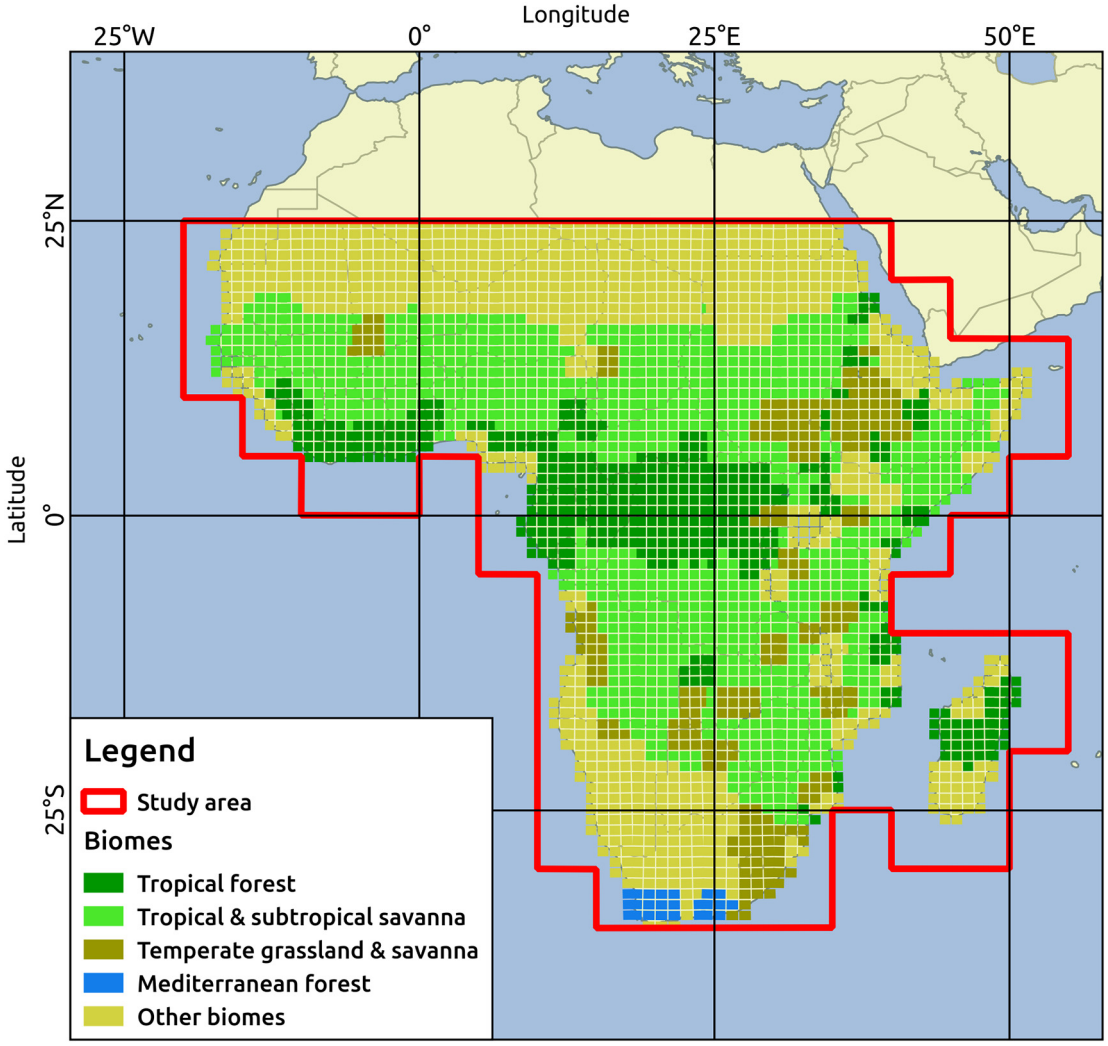

Fig. 1. Biome distribution for the study area according to Olson et al. (2001) for the Copernicus Sentinel-2 tiling system.

GLOBSCAR (Simon et al., 2004), both from European sensors, which were followed by the Globcarbon (Plummer et al., 2006), L3JRC (Tansey et al., 2008), and more recently by the Copernicus Land Burned Area. The first NASA BA product was based on the MODIS sensors: MCD45A1 (Roy et al., 2008) and more recently the MODIS MCD64, which is now the standard NASA BA product (last version released is collection 6: Giglio et al., 2018). From the previous version of this product (c5), the burned component of the Global Fire Emissions Database-GFED was delivered (Giglio et al., 2010). Within the European Space Agency (ESA)'s Climate Change Initiative, several global BA products have been recently releases: FireCCI31 and FireCCI41, based on the MERIS sensor (Alonso-Canas and Chuvieco, 2015), and FireCCI50, based on MODIS 250 m red and near infrared reflectances (Chuvieco et al., 2018).

All currently existing global products are based on coarse spatial-resolution sensors including MERIS (300 m), MODIS (250 m–500 m) and AVHRR or VEGETATION (around 1000 m). With those pixel sizes, detection of small fires (< 100 ha) becomes very challenging. Although small fires are usually less catastrophic than large fires, they still play a significant part in land use transformation and total emissions from fires, particularly in tropical regions, where fires tend to be human driven, either for agricultural expansion, grazing purposes or hunting (Grégoire et al., 2013; Hantson et al., 2015). Extrapolating relations between active fires and small burn patches, Randerson et al. (2012) estimated that 26% of the global BA was the result of small fires, which would imply increasing total BA area by 1.2 M km^2/year. The same study estimated that 24% of African BA came from small fires (0.78 M km^2/year). However, Hantson et al. (2013) has shown that active fires may have missed up to 80% of all fires in tropical regions, which add up to 50% of the total BA. Additionally, when comparing the accuracy of different global BA products (MCD45A1, MCD64A1 and FireCCI31) with reference perimeters derived manually from Landsat data, omission errors showed to be higher than 65% for the tested products (Padilla et al., 2015). All these omissions cause an underestimation on the greenhouse gas emissions to the atmosphere, which should improve if small burned areas were taken into account.

The increasing availability of medium spatial resolution sensors such as Landsat-OLI (30 m) or Sentinel-2 Multi Spectral Instrument (MSI) (10 m) may soon overcome those limitations to detect smaller fires, making possible a more accurate estimation of global BA. Several local/regional burned area algorithms based on Landsat TM/ETM+ images were developed in the last decade (Bastarrika et al., 2011; Goodwin and Collett, 2014; Stroppiana et al., 2015, 2012). Only recent studies have suggested the use of medium resolution sensors to generate global BA products. This was the case of the MODIS-Landsat data fusion product by Boschetti et al. (2015), or the US conus BA product generated from Landsat historical archives (Hawbaker et al., 2017). One of the main limitations of using these sensors for BA mapping is their poor temporal resolution (8 days if both Landsat-7 and 8 are used), which makes BA detection in tropical ecosystems challenging, due to

significant cloud cover and short post-fire signal persistence. With the launch of the two Sentinel-2 missions and a 5-day revisiting frequency (at the equator), this problem will be mitigated, even more if the Landsat-8 and Sentinel-2 data are integrated.

In this paper we present a new BA algorithm adapted to MSI characteristics and its implementation on a very large area and an entire fire season to test the operational potential for producing continental scale BA datasets from S-2 MSI data. This algorithm was developed in the framework of the Climate Change Initiative programme of the ESA. For this reason, we have selected the Sub-Saharan Africa (SSA) region as study case, as it is the most burned continent and produces the larger gas emissions (Chuvieco et al., 2018; Van Der Werf et al., 2017). The whole 2016 year was processed, including the whole fire season in Southern Hemisphere Africa (SHAF), and two half fire seasons in the Northern Hemisphere (NHAF).

2. Methods

2.1. Study area

The BA Algorithm for the MSI sensor has been tested in the SSA (Sub-Saharan Africa) covering the latitudes from 25°N to 35°S (Fig. 1). Although fires affect a variety of ecosystems and locations, the current/existing global BA products showed that Africa is the most affected continent by biomass burning, comprising up to 70% of all the area burned worldwide (Chuvieco et al., 2016, 2018; Giglio et al., 2013). Fires occur in the corresponding dry season in both the Northern and Southern Hemispheres, being these seasons from October to March north to the Equator and from May to October in the south. Although African fires show a strong variability, particularly in seasonal and daily cycles, most fires detected by Terra and Aqua MODIS (around 90%) were detected during the day (Giglio et al., 2006a). Fires are also affected by land cover changes as the transformation of natural vegetation to croplands, decreasing the total burned area after the conversion (Grégoire et al., 2013).

Most fires in this region are caused by human activities for the management of crops, grazing and hunting (Grégoire et al., 2013; Lewis et al., 2015). This area includes several biomes (Olson et al., 2001): tropical forest (especially around the equator), tropical and subtropical savanna (in subtropical areas), temperate grassland and savanna, Mediterranean forest (in southern Africa), and other residual biomes (mainly arid regions).

2.2. Data

2.2.1. Active fire data

Several BA algorithms combine detection of hotspots and changes in reflectance over time to better discriminate burned pixels, as the thermal contrast of fires is often more noticeable than their impact on reflectance changes (Alonso-Canas and Chuvieco, 2015; Boschetti et al., 2015; Fraser et al., 2000; Giglio et al., 2009; Giglio et al., 2006b; Pereira et al., 2017). Active fire data for development of the BA algorithm were obtained from the Moderate Resolution Imaging Spectroradiometer (MODIS) sensor, comprising 1 km detections from the combined 4 overpasses of the sensor on the Aqua and Terra satellites. The precise coordinates of the hotspots were downloaded from the Fire Information for Resource Management System (FIRMS) (https://firms.modaps.eosdis.nasa.gov/download/, last accessed on November 2018). The data come from the Collection 6 Near Real Time (NRT), extracted from the standard MCD14ML fire product produced at the MODIS Fire Science Computing Facility (SCF). Active fires were not filtered depending on the quality layer.

2.2.2. Copernicus Sentinel-2 MSI

Sentinel-2 (S2) is an Earth observation mission developed by ESA as part of the Copernicus Programme to acquire terrestrial observations in support of environmental services and natural disaster management (Drusch et al., 2012). The mission includes two identical satellites, S2-A (launched in June 2015) and S2-B (launched in March 2017), providing complementarity for the current SPOT and Landsat missions. The main sensor is the MultiSpectral Instrument (MSI), a pushbroom scanner that provides a wide spectral coverage over the visible, near infrared (NIR) and short-wave infrared (SWIR) domains (amounting to 13 spectral bands), with medium spatial resolution (from 10 m to 60 m depending on the wavelength) and a wide field of view (290 km) (ESA, 2011) (https://earth.esa.int/documents/247904/685211/Sentinel-2_User_Handbook, last accessed on November 2018). This makes possible a global coverage of the Earth's land surface (between 56°S and 83°N latitudes) every 10 days with one satellite and every 5 days with 2 satellites. In this analysis only S2-A data were used because S2-B data were not yet available when we started the processing of the BA product.

The input data for our BA algorithm was the Level-1C product. This product includes Top-Of-Atmosphere (TOA) reflectances with sub-pixel multispectral registration in UTM projection and WGS84 geodetic system in tiles of 100 × 100 km. The data were downloaded from the Sentinel Scientific Data Hub (https://scihub.copernicus.eu, last accessed on November 2018), free of charge. The images were atmospherically corrected using the algorithm 'sen2cor' v2.2.1 issued as part of the standard Sentinel-2 Toolbox (downloadable from http://step.esa.int/main/third-party-plugins-2/sen2cor/, last accessed on November 2018). This algorithm generates Bottom of Atmosphere (BOA) reflectance images, as well as several products such as Aerosol Optical Thickness, Water Vapor and Scene Classification maps (SCL). From these layers, only SCL was used to mask defective pixels and clouds.

2.3. Spectral analysis

A spectral sensitivity analysis was carried out as a first step for the BA algorithm development to determine which bands and/or spectral indices were the most suitable for BA detection. Reference perimeters from 2016 located in 52 S2 tiles systematically distributed through all Africa were visually created using BAMS (Burned Area Mapping Software) methodology (Bastarrika et al., 2014), which consists in a trained classification to detect burned areas between images from two dates.

For each reference location 20,000 random sample points were extracted from burned and unburned categories to analyze their spectral distribution (10,000 samples for each category). The unburned class contains every pixel that could not be classified as burned, water, cloud or cloud shadow: urban areas, bare areas, unburned vegetated areas, and even burned areas that were already burned in the pre-fire date. The spectral sensitivity analysis was computed for 9 MSI bands (all bands processed at 20 m by sen2cor) as well as several common spectral indices used in BA algorithms (Bastarrika et al., 2011; Chuvieco et al., 2002; Huang et al., 2016; Smith et al., 2007; Stroppiana et al., 2012; Veraverbeke et al., 2011), covering the Visible/NIR, the NIR/Short SWIR and the Short SWIR/Long SWIR spectral spaces:

- Visible/NIR space: Enhanced Vegetation Index (EVI) (Huete et al., 1994), Normalized Difference Vegetation Index (NDVI) (Rouse et al., 1974), Global Environment Monitoring Index (GEMI) (Pinty and Verstraete, 1992), Burned Area Index (BAI) (Martín and Chuvieco, 1998), Soil-Adjusted Vegetation Index (SAVI) (Huete, 1988).
- NIR/SWIR space: Modified Burned Area Index (BAIM) (Martin et al., 2005), Normalized Burn Ratio (NBR) (Key and Benson, 1999).
- Long SWIR/Short SWIR space: Mid-Infrared Burned Index (MIRBI) (Trigg and Flasse, 2001), Normalized Burned Ratio 2 (NBR2) (García and Caselles, 1991).

Spectral sensitivity analyses were performed for both post-fire

values and multitemporal differences (post-fire and pre-fire values subtraction). Both parametric and non-parametric analyses were carried out, as recommended by different authors (Gómez et al., 2016; Huang et al., 2016). The parametric separability index (M) that was defined as follows (Kaufman and Remer, 1994; Lasaponara, 2006; Smith et al., 2007):

$$M = \frac{|\mu_b - \mu_{ub}|}{\sigma_b + \sigma_{ub}} \quad (1)$$

where μ_b and μ_{ub} are the mean values of burned and unburned samples and σ_b and σ_{ub} the corresponding standard deviations. The separability between classes is generally considered poor when the M index is lower than 1, while M higher than 1 indicates a good separability (Kaufman and Remer, 1994).

The non-parametric analysis was based on the Random Forest (RF) Classifier, which provides an importance score for each input variable (https://scikit-learn.org/stable/modules/generated/sklearn.ensemble.RandomForestClassifier.html, last accessed on November 2018). This score measures the total decrease in node impurity averaged over all tress of the ensemble and can be used to rank the importance of that variable in relation to the others in the classification.

The results shown in Fig. 2 are the averages of the values of 52 S2 tiles where reference perimeters were generated.

The Mid-Infrared Burned Index (MIRBI, Eq. (2)) and the Normalized Burned Ratio 2 (NBR2, Eq. (3)) were found to have the highest M value between burned and unburned categories, and this behaviour is also confirmed with the RF importance score.

$$MIRBI = 10 \cdot \rho_{SWIRL} - 9.8 \cdot \rho_{SWIRS} + 2 \quad (2)$$

$$NBR2 = \frac{\rho_{SWIRS} - \rho_{SWIRL}}{\rho_{SWIRS} + \rho_{SWIRL}} \quad (3)$$

where ρ_{SWIRL} and ρ_{SWIRS} are, respectively, Short Wave Infrared Long reflectance and Short Wave Infrared Short reflectance, both adimensional, and corresponding to B12 and B11 bands of MSI sensor.

Both indices were finally selected for the BA algorithm definition, although they rely on the same spectral bands (Short and Long SWIR bands, B11 and B12 for S2 images) because of the different distributions of the burned/unburned category (Fig. 3), being NBR2 much more homogeneous; this different behaviour is important when defining the contextual stage of the algorithm when defining background (not burned)/foreground (burned) cut-off values to maintain low commission errors. The ability of the SWIR bands when emphasizing the burned/unburned in African environments has previously been noted, as they are less influenced than the visible bands by scattering and are well associated to post-fire impacts (Pereira et al., 1999; Smith et al., 2007).

Apart from NBR2 and MIRBI, the NIR variable was also selected (B8A band for MSI images): adding post variables is important to reduce changes not related to fire (specially for differentiate from croplands) and this variable is shown to be one of the most significant with the second M higher value (after MIRBI) and the fourth higher RF score (after the BAI index that it is highly correlated with the NIR). The NIR spectral region is known to play an important role when mapping burned areas and is also the most stable along ecosystems (Huang et al., 2016; Pereira et al., 1999).

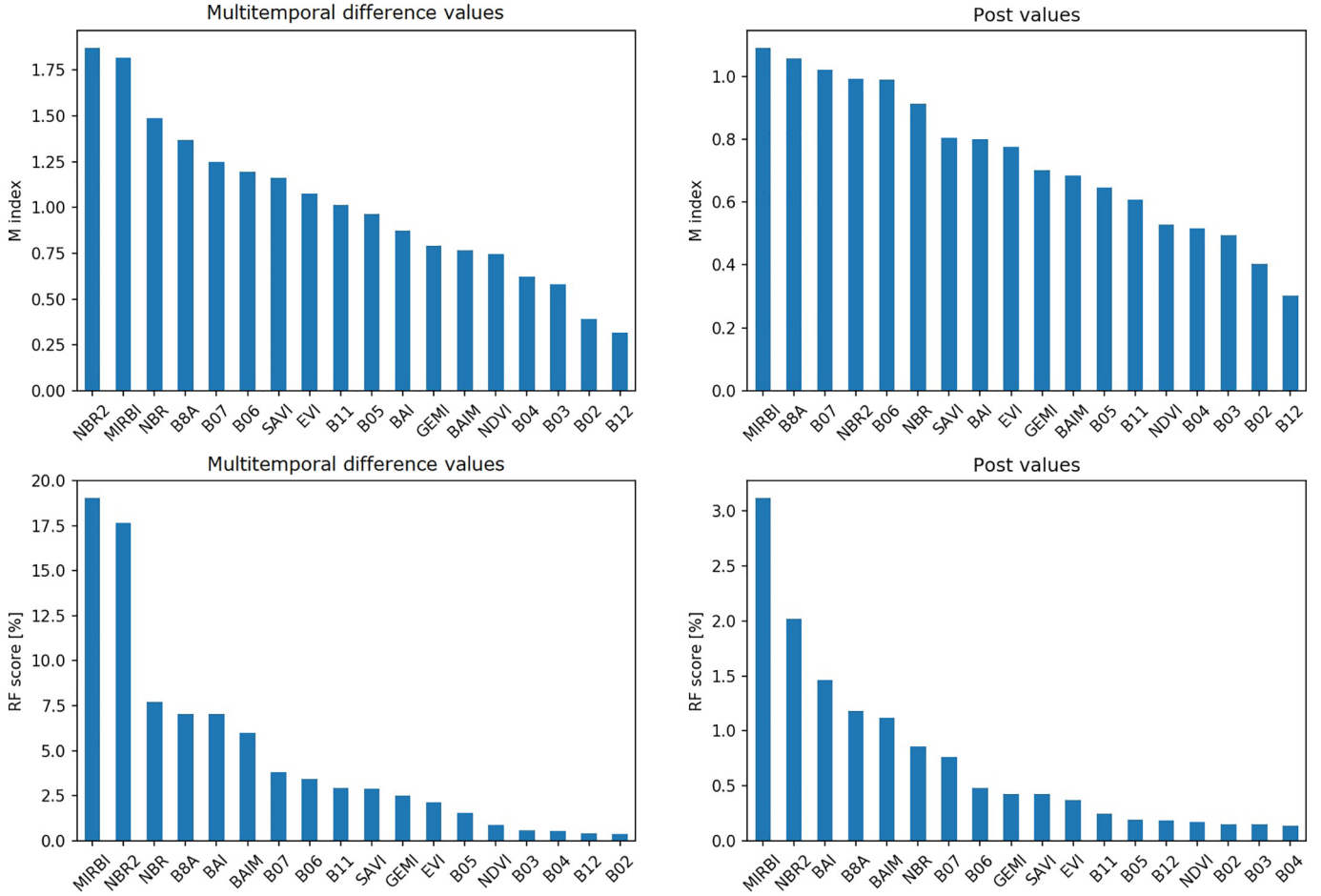

Fig. 2. M separability index (first row) and Random Forest importance score (second row) mean values from 52 reference tiles sorted in descending order. The left column shows the multitemporal difference variables while the right column shows the post-fire values.

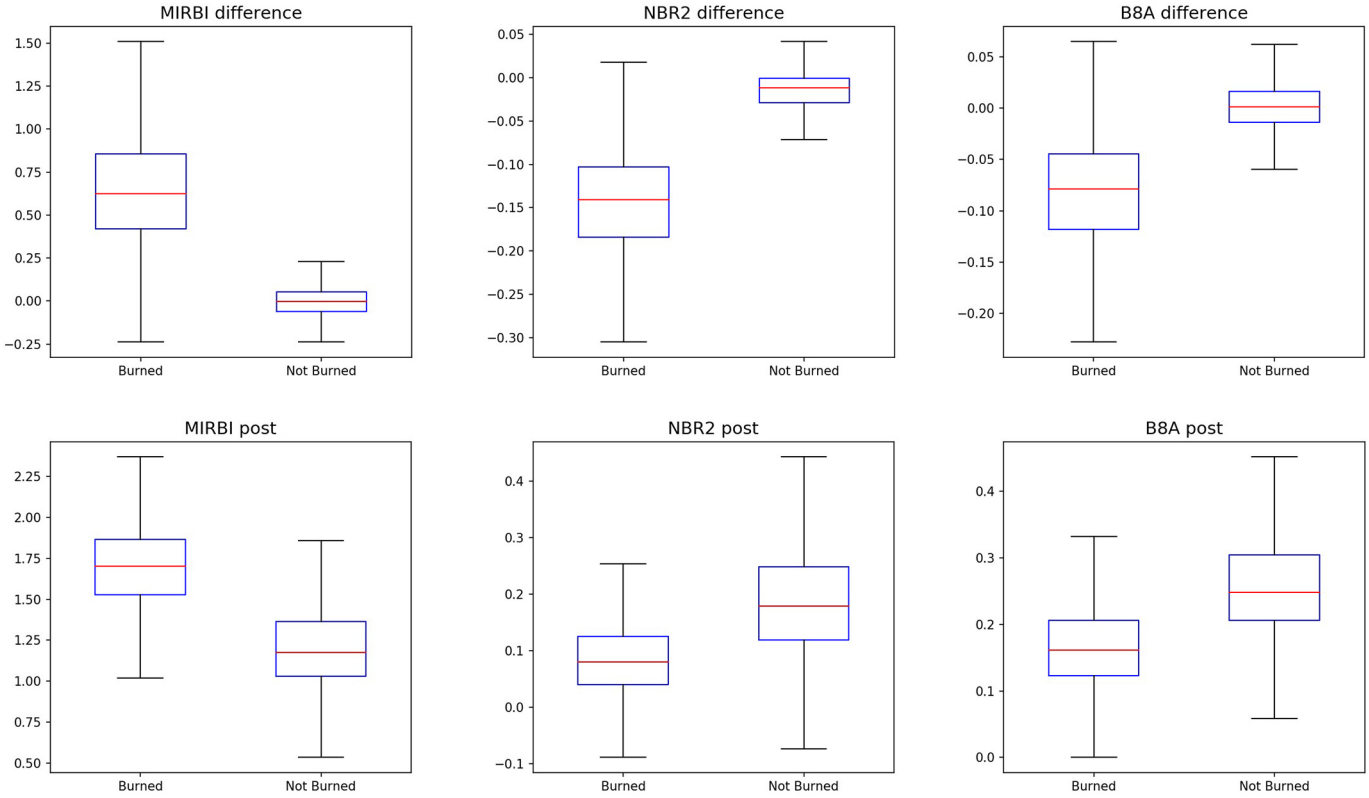

Fig. 3. Spectral distribution of burned and unburned categories for MIRBI, NBR2 and NIR multitemporal difference and post-fire values.

2.4. Algorithm

2.4.1. General overview

The proposed BA algorithm compared two consecutive Sentinel-2 acquisitions by calculating burned probability using MIRBI and NBR2 spectral indices and the NIR band derived from the L2A product (Fig. 4). The algorithm estimated an initial BA based on fixed thresholds, which were overlaid with the MCD14ML hotspots detected between the time-lapse of the two MSI acquisitions in order to define the regions with a very high likelihood of being burned. Those BA areas confirmed by hotspots were used to obtain tile dependent statistical thresholds for each predictive variables in a two-phase burned strategy, following a modified method from Bastarrika et al. (2011).

A mask of 'not burnable' areas was produced using the Scene Classification Layer (SCL) generated by 'sen2cor', corresponding mostly to unobserved areas (clouds and cloud shadows) and water bodies. The pixels that satisfy the following criteria were masked out for further processing:

- No data, saturated pixels, water and snow.
- Medium-high probability clouds and thin cirrus with a dilation of 5 pixels (100 m) were used in order to obtain a more robust cloud mask, to be applied to the image pair under consideration (low probability clouds were not classified as not burnable, since they included a very significant quantity of burned areas).
- Dark area pixels and cloud shadows of the SCL were not used on the mask for the same reason as low probability clouds and because many burned pixels in the savannas fall in these categories. A fixed criterion based on the post-fire [t_2] Long SWIR band (B12) was used instead. Burned areas and shadows were well separated by a reflectance value of 0.07, so pixels where B12 < 0.07 were considered cloud shadows and therefore removed from further processing.

2.4.2. Hotspots confirmed burned pixels (HCBP)

In the first stage of the algorithm a set of burned pixels that satisfied a fixed criteria were selected, whence tile based statistics could be used at the second stage. To ensure initially detected pixels were in fact burned, they had to fulfill certain conditions (described below) and had a MODIS hotspot in the neighborhood. All the hotspots, regardless the detection confidence and sensing angle were selected because they were only used to confirm the spectral change observed in the Sentinel-2 imagery.

Assuming two consecutive Sentinel 2 tiles ([t_1] and [t_2]), a pixel was labeled as Hotspots confirmed burned pixels (HCBP) if it satisfied all the following conditions:

- MIRBI ([t_2]) $>$ tile mean MIRBI ([t_2])
- MIRBI difference ([t_2] $-$ [t_1]) > 0.25
- NBR2 ([t_2]) $<$ tile mean NBR2 ([t_2])
- NBR2 difference ([t_2] $-$ [t_1]) < -0.05
- NIR ([t_2]) $<$ tile mean NIR ([t_2])
- NIR difference ([t_2] $-$ [t_1]) < -0.01
- It had a MODIS hotspot in between ([t_1]) and ([t_2]) in the 1000 m vicinity of that pixel
- It was part of a patch larger than 30 ha (750 pixels), which was observed to be the minimum area necessary to assure that it was actually a burned patch and no other unburned artifacts.

The thresholds for MIRBI, NBR2 and NIR multitemporal difference (0.25, -0.05 and -0.01 respectively) were obtained analyzing the cut-off points of the probability distributions of the burned and unburned category at the 52 reference sites cited in Section 2.3. For the post-fire variables, the mean of the whole tile was selected as threshold, obtaining and adaptive thresholds that helped reducing the commission errors of those pixels that fulfilled the multitemporal criteria (for example at croplands).

The aim behind this first stage of the algorithm was to obtain a set of

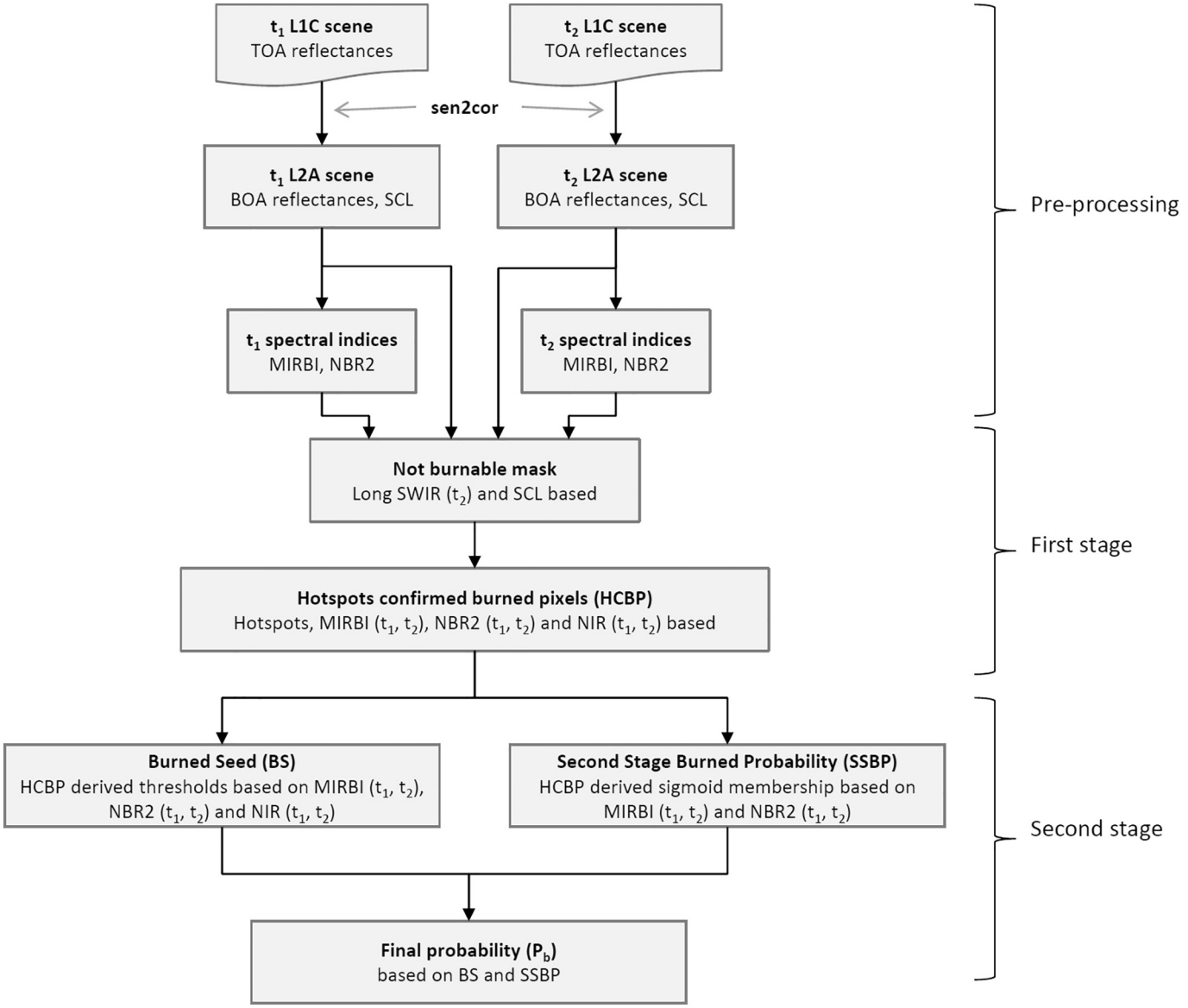

Fig. 4. Flowchart of the BA algorithm applied to two time-consecutive S-2 acquisitions.

pixels highly likely to be burned given that an active fire was observed in the vicinity, and a spectral change according to a fire event was shown. The remaining pixels were considered as unburned pixels. This initial classification was used to have foreground (burned) and background (unburned) probability distributions for each tile and period that were used in a following two-stage process.

2.4.3. Burned seeds (BS)

Burned seeds (BS) were obtained assigning as thresholds the 5thand 95thpercentiles of HCBP, depending on whether a particular variable higher or lower the values after a fire, respectively. A pixel was identified as a BS if it satisfied all the following rules:

- MIRBI ($[t_2]$) > MIRBI 5th percentile HCBP ($[t_2]$)
- MIRBI difference ($[t_2] - [t_1]$) > MIRBI 5th percentile HCBP ($[t_2]$-$[t_1]$)
- NBR2 ($[t_2]$) < NBR2 95th percentile HCBP ($[t_2]$)
- NBR2 difference ($[t_2] - [t_1]$) < NBR2 95th percentile HCBP ($[t_2]$-$[t_1]$)
- NIR ($[t_2]$) < NIR 95th percentile HCBP ($[t_2]$)
- NIR difference ($[t_2] - [t_1]$) < NIR 95th percentile HCBP ($[t_2]$-$[t_1]$)

2.4.4. Second stage probability of burn (SSPB)

The second stage probability of burn (SSPB) was focused on reducing the omission error (Bastarrika et al., 2011) and it was based exclusively on MIRBI and NBR2 multitemporal difference variables given that they had shown a much higher importance than the post-fire variables according to the RF score. For the same reason the NIR variable was not introduced either to avoid increasing omission errors.

The main purpose in this stage was to define a mathematical function that would make the transition from 0% (unburned pixels) to 100% (burned pixels) probability. A logistic function was used for this purpose, which provided a smooth transition between the two classes. This approach was already used in other BA studies (Bastarrika et al., 2011; Fraser et al., 2002; Koutsias and Karteris, 2000; Pu and Gong, 2004). The logistic functions for MIRBI and NBR2 differences are s-shaped and z-shaped, respectively, to reflect the fact that the former increases its values when an area is burned while the latter decreases (Fig. 5). To calculate the lower and upper boundaries on the logistic curve, corresponding to 0% and 100% probabilities, different percentiles were extracted from the sets of burned and unburned pixels of HCBP. 90th (MIRBI difference) and 10th (NBR2 difference) percentiles of unburned pixels were set as the 0% probability, and the 50th percentile of burned

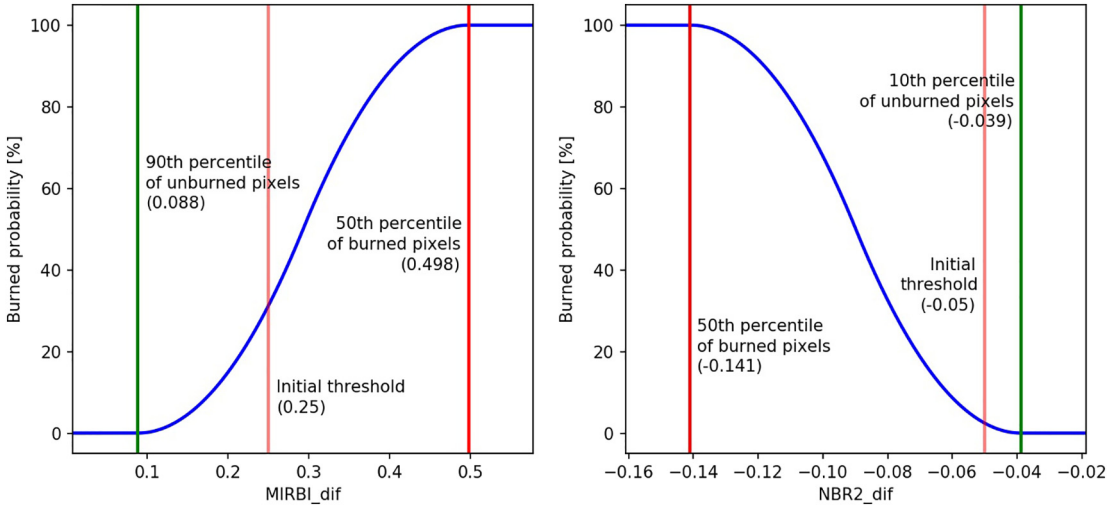

Fig. 5. Two sample logistic curves, with the s-shape for MIRBI difference and z-shape for NBR2 difference, taken from tile 28PET, period December 22, 2015/January 11, 2016. The initial thresholds are those extracted from the spectral analysis and applied to HCBP.

pixels was used for the 100% value. There is no symmetry between the percentiles of both categories; anomalies were found in the set of burned pixels when it was formed by a limited number of pixels, so a more "central" percentile (50th, the median) is used to avoid this effect.

The final second stage probability of burn (SSPB) was obtained by multiplying them, considering MIRBI and NBR2 probabilities were independent.

2.4.5. Final burned probability map

The BS and SSPB image were used to get the Final Burned Probability Map (FBPM) in a two-step focus trying to balance omission and commission errors. Unlike in Bastarrika et al. (2011), the two step process in this algorithm did not use a region growing method but a cost-path based approach as the SSPB image is a continuous space. For each SSPB pixel higher than 0 probability value, the final burned probability was the minimum probability of the route crossing probabilities as high as possible from that pixel towards the BS. If pixel near a seed was considered, the probability was high (the minimum probability that crossed the path between both is high), while when that pixel was far away from the seeds, that probability tended to be low given that crossed low probability burned regions.

2.4.6. Temporal application of the algorithm

Extending the temporal application of the algorithm (the definition until now has been limited to two consecutive scenes named [t_1] and [t_2]), the final set of burned pixels was created by comparing each image [t_n] to the preceding four acquisitions [t_{n-1}, t_{n-2}, t_{n-3}, t_{n-4}]. The main objective was to fill unobserved areas (masked as detailed in Section 2.4.1) in the previous images. This gap filling process is illustrated in Fig. 6 (although with only 3 pre-fire dates). If the acquisition at [t_n] were compared only with the first preceding image ([t_{n-1}]), most burned pixels hidden by clouds in the [t_{n-1}] image would have been masked and they wouldn't be included in the final BA product. Taking into account more preceding images as comparison source the masked areas were filled using the latest pre-fire reference. Only the pair of images with > 5 km^2 (12,500 pixels) of observed (unmasked) areas and at least one active fire between the two dates were processed to improve the computation performance and avoid acquisitions with a higher probability to commit commission errors; otherwise it was assumed that it did not contain any burned pixel within that period.

2.4.7. Processing environment

The described BA algorithm was implemented on Calvalus processing system developed by Brockmann Consult Gmbh, Germany (http://www.brockmann-consult.de/calvalus, last accessed on November 2018). The pre-processing consisted on running 'sen2cor' processor for 11,054 S2 MSI tiles, amounting for 63 TB of data. This process took about 9 weeks. Additionally, four months were required to run the BA algorithm for the whole 2016 year, totaling additional 87 TB of processed data (including intermediate files). The final product was named FireCCISFD11 (version 10, included a preliminary version covering just the northern hemisphere of Africa, but it was only released to a few climate users).

2.4.8. Threshold between burned and unburned areas

The confidence values for each pixel were obtained from the probability distribution functions. Given that the result of the BA algorithm was a continuous image (with confidence levels from 0% to 100%) but reference perimeters were discrete (burned/unburned), a fixed threshold was established to convert the classification outputs into a binary layer. Different values were tested to balance omission and commission estimations based on the 52 tiles that were used for selecting the most sensitive bands for the algorithm (see Section 2.3). Analyzing the distribution of omission, commission and Dice coefficient values in those 52 sites, 5% was found to be the best threshold (see 34PET example in Fig. 7). This low cut-off value was related to the percentiles values used in Section 2.4.4, whose asymmetry caused the logistic curves to be closer to the burned area, and to the multiplication of MIRBI and NBR2 probabilities at the SSPB stage. No cut-off value was used for the MCD64A1 product.

2.5. Validation

BA reference data were generated for a statistically derived sample of validation sites, and compared with the FireCCISFD11 for its assessment. The validation was also carried out with the now standard NASA BA product: the MCD64A1 collection 6, derived from MODIS data (Giglio et al., 2018, 2009), as this product is widely used by atmospheric and carbon modellers. This global product was derived from high temporal resolution data (daily Terra and Aqua acquisitions, compared to 10 days of S-2 acquisitions) but at much lower spatial resolution than the FireCCISFD11 product (500 versus 20 m). Intercomparison of FireCCISFD11 and MCD64A1 products was also carried out, to analyze the seasonal and spatial differences between the two products.

Reference perimeters were generated from multi-temporal comparison of Landsat imagery following standard CEOS CalVal validation protocols (Boschetti et al., 2009). Given the different temporal

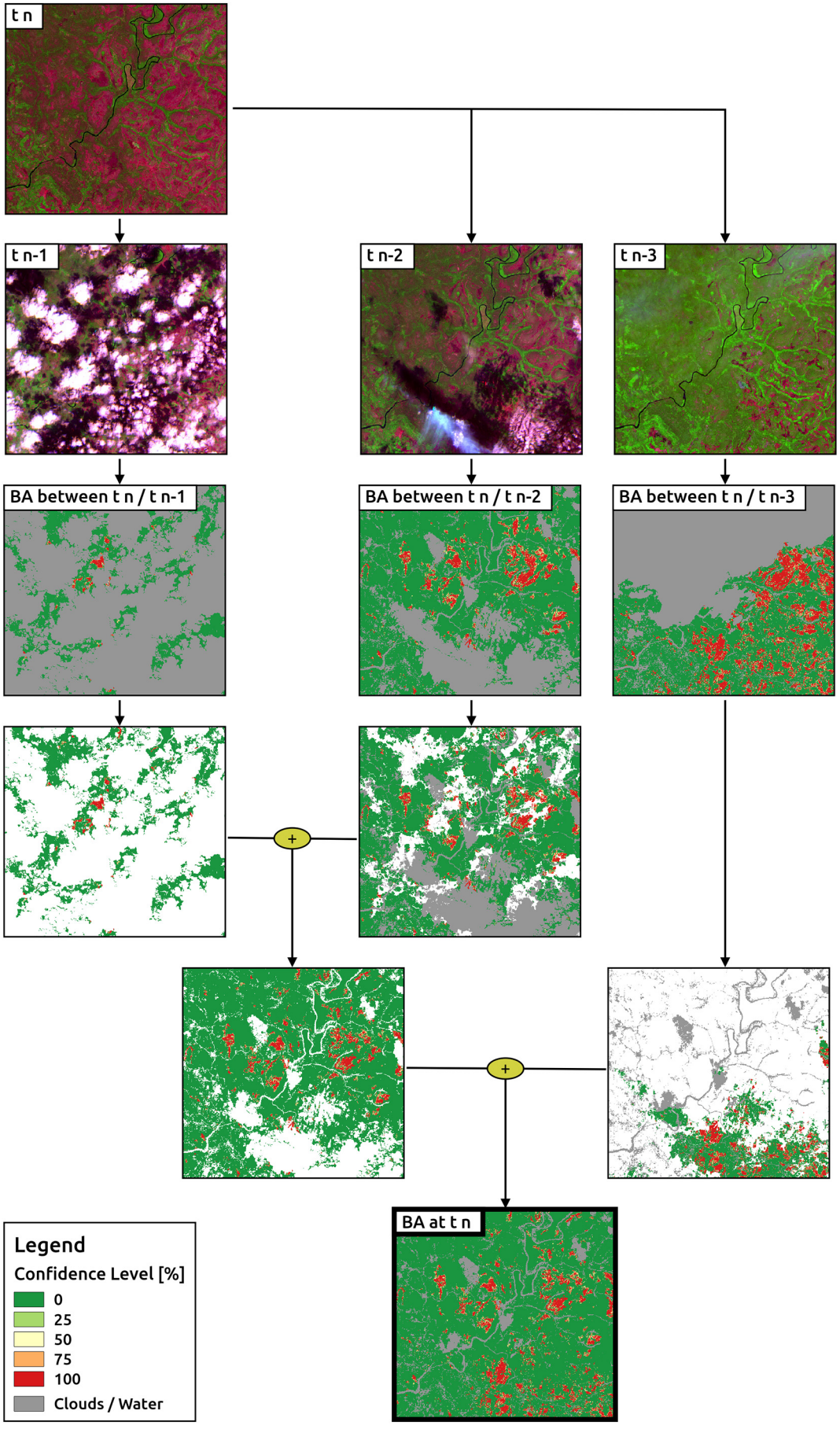

(caption on next page)

Fig. 6. Example of the temporal application of the BA algorithm in a sample area, comparing one post-fire date ([t_n]) with 3 previous pre-fire dates ([t_{n-1}], [t_{n-2}] and [t_{n-3}]). The first two rows show SWIR-NIR-Red colour composites for individual dates; the third row shows resulting burned areas using three consecutive precedent pre-fire images. The figure illustrates how cloudy areas are filled with BA detected from previous pre-fire images, being the last aggregation the final BA detected by the algorithm for the post-fire date ([t_n]). Even though the post-fire image in this example is compared with 3 pre-fire images, 4 pre-fire dates are used in the algorithm. (For interpretation of the references to colour in this figure legend, the reader is referred to the web version of this article.)

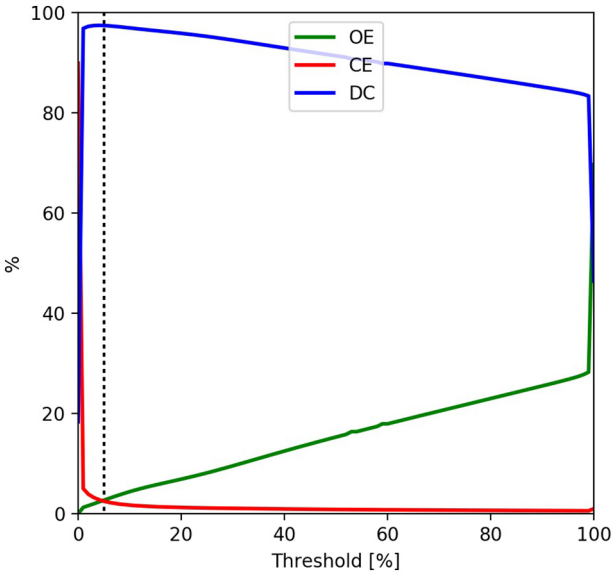

Fig. 7. Evolution of omission and commission errors and the Dice coefficient depending on the threshold applied to the FireCCISFD11, in a sample tile (34PET).

resolutions of both the product and reference perimeters, which cause inevitable differences between dates, temporally *long sampling units* of around 115 days (depending on data availability) were designed to allow a good overlap of reference perimeters with the product. Validation sites were selected from Landsat 7 and 8 scenes following similar criteria to Padilla et al. (2015, 2014). Olson biomes (Olson et al. (2001) and historical fire occurrence were used as stratification criteria. 45 random *long sampling units* were selected (Fig. 8). Every validation site was subsampled using a 30 × 20 km window located in the centre of the scene to increase sampling efficiency and simplify visual inspections in the reference perimeters generation process.

Reference perimeters were created between all pairs of consecutive images. First training polygons were digitized for burned and unburned classes (plus cloud or cloud shadows when needed), which were used to train a RF Classifier with NBR, SWIR and NIR of both dates and the multitemporal NBR difference as input variables. After this semi-automatic mapping of burns, a systematic quality control was performed through visual inspection and training polygons were modified and classification re-run where necessary. This procedure was iterated until no errors were identified.

The validation of both FireCCISFD11 and MCD64A1 products was carried out by estimating the error matrix for each validation site, obtaining the omission (OE) and commission (CE) error ratios for the burned category. The Dice coefficient (DC), which is a measure of accuracy that has a probabilistic meaning (Dice, 1945; Padilla et al., 2015), was also computed; it is defined as the probability that given that one product (the BA product or the reference perimeters) identifies a pixel as burned, the other product will also identify it as burned (Fleiss, 1981). Relative bias (relB) was also computed, as it indicates if BA are overestimated or underestimated in the product. Since the spatial resolution is different for each product (20 and 500 m) and

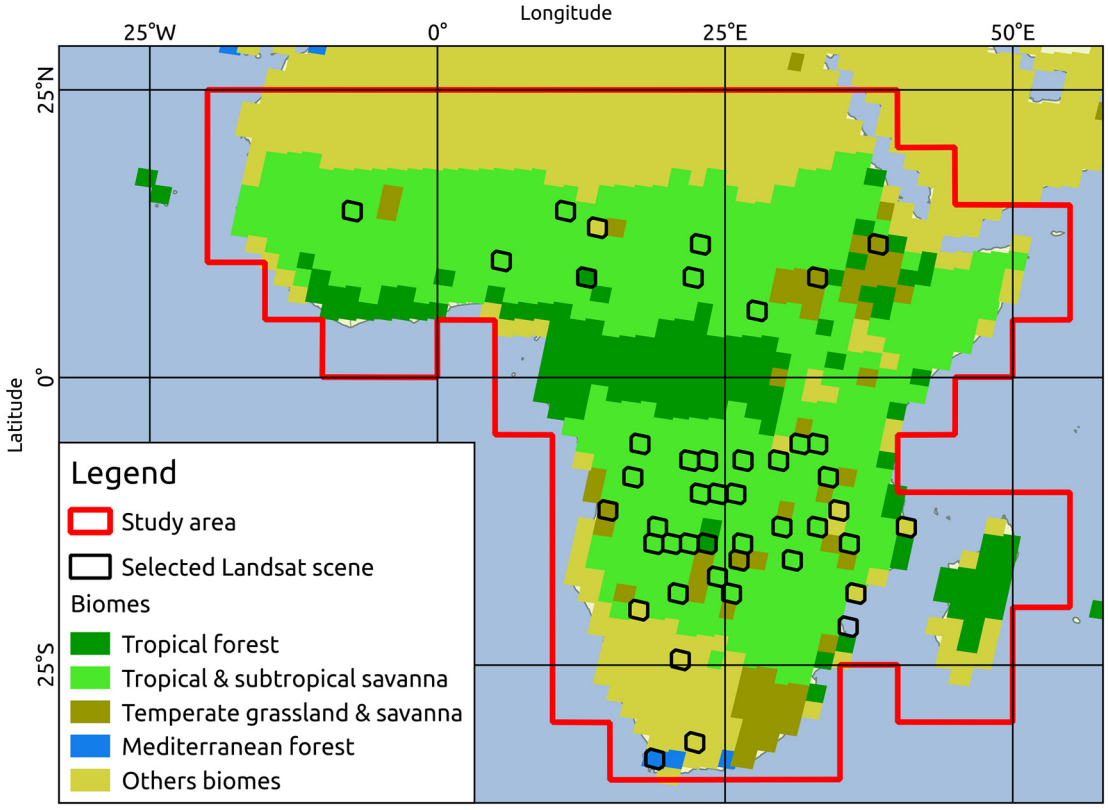

Fig. 8. Location of selected Landsat scenes.

Table 1
Estimated accuracy of the FireCCISFD11 product, in *long* and *short sampling units*. Commission error (CE), omission error (OE), Dice coefficient (DC) and relative bias (relB) are expressed in percentages.

	Commission error (CE)	Omission error (OE)	Dice coefficient (DC)	Relative bias (relB)
Long sampling unit	19.3	26.5	77.0	−9.0
Short sampling unit	64.1	67.4	34.2	−9.0

reference perimeters (30 m), the error matrices were computed by comparing the results as vectors rather than raster images.

All these accuracy measures were computed twice: once for individual pairs of consecutive images (called *short sampling unit*, up to 16 days long), and again for temporal series with consecutive image pairs (called *long sampling unit*, 100 days long at least, 45 in total).

3. Results

3.1. Validation of the FireCCISFD11

The results of the accuracy measures after comparing the FireCCISFD11 product and the validation dataset are shown in Table 1. At *long sampling unit*, omission error (26.5%) is higher than commission error (19.3%), giving a negative relative bias (−9.0%) and a Dice coefficient of 77.0%. At *short sampling unit* both omission and commission sharply increase to over 60%, while DC decreases to 34.2%. The relative bias remains the same, since the total burned surface does not change between a long sampling unit and the sum of corresponding short sampling units. The much lower accuracy of the *short sampling unit* is related to the temporal differences of the acquisitions dates between Landsat (validation source) and Sentinel-2 images.

3.2. Validation of MCD64A1

Table 2 shows the same accuracy measures after comparing the MCD64A1 product and the validation dataset. At *long sampling unit*, omissions (59.6%) were found much higher than commission (20.4%), with a negative relative bias (−49.2%) and Dice coefficient of 53.6%. At *short sampling unit* omission (66.3%) and commission (33.6%) were slightly higher getting 44.7% Dice coefficient.

3.3. Inter-comparison of FireCCISFD11 and MCD64A1

3.3.1. Total BA

Burned area detected by FireCCISFD11 and MCD64A1 were compared in a monthly basis and taking into account the sizes of the burned patches grouped in different fire size classes: < 25 ha, 25–100 ha, 100–250 ha and > 250 ha (Figs. 9 and 10). The total BA detected in the FireCCISFD11 for the whole year 2016 (4.9 M km^2) was 80% larger than the area detected by the MCD64A1 product (2.7 M km^2), being larger on every month (Fig. 9). BA were concentrated between October and March in the Northern Hemisphere (2.3 and 1.3 M km^2 for the FireCCISFD11 and MCD64A1 products, respectively), followed by several months with a reduced fire activity, while in the Southern Hemisphere the highest detection was observed between May and October (2.6 and 1.4 M km^2 for the FireCCISFD11 and MCD64A1 products, respectively).

Both FireCCISFD11 and MCD64A1 products detect a similar BA area regarding to the largest burned patches (> 250 ha) (Fig. 10), but the differences between products increase gradually as the patch size decreases. The maximum difference was observed for the smallest fire patches (< 25 ha), that were detected by FireCCISFD11 more than thirty times more than by the MCD64A1 for patches equal or < 25 ha. Note that the MODIS minimum detectable area (a pixel) is 25 ha.

3.3.2. Spatial agreement

The fraction of burned area in a 0.05 × 0.05° resolution was aggregated to compare the spatial agreement between FireCCISFD11 and MCD64A1 products (Fig. 11). Both products are shown as well the BA fraction difference between them. Fig. 11d shows the regression between the BA fraction between both products (note FireCCISFD11 is in X axis, and MCD64A1 in Y axis). FireCCISFD11 tends to detect larger burned area than the MCD64A1; the slope of the regression line is lower than 1.0 (0.703) and Fig. 11c shows in general a blue colour that notes the positive fraction difference. Higher burned fractions in the MCD64A1 product were observed when the FireCCISFD11 was not able to detect burned areas because of the high cloud percentage, mostly noticeable at the end of the 2016.

According to Table 3, where correlation is grouped by patch size, very low spatial correlation between the two products was found for patches below 250 ha (R^2 < 0.1), while larger patches showed a much higher correlation (R^2 equal to 0.571), with a regression slope of 0.871 that notes the lower BA fraction values of MCD64A1.

Figs. 12 and 13 illustrate the differences among products in two representative sample sites. The first one (Fig. 12), located in Senegal (tropical and subtropical savanna ecosystems), affects shrublands and tree cover according to the ESA CCI Land Cover map from 2015 (http://maps.elie.ucl.ac.be/CCI/viewer/index.php, last accessed on November 2018). This sample site contains large BA detected with similar shapes by both BA products, though smaller areas were only detected by the FireCCISFD11. Most burned patches were detected later in the FireCCISFD11 than in the MCD64A1 due to its lower temporal resolution, but no significant differences were observed. The second (Fig. 13) sample site, located in Zambia (temperate grassland and savanna ecosystems) affects mostly irrigated croplands and tree covers (ESA CCI Land Cover map). In this case fires tend to be small size, with a very clear underestimation of the MCD64A1; correspondences are only found for largest patches.

3.3.3. Temporal agreement

The temporal accuracy of the BA detection date was analized comparing to de detection dates of the FireCCISFD11 and MCD64A1 against the hotspot MCD14ML acquisition dates. The date of burn chosen in the products was the earliest burned pixel around the hotspot (in a 1 × 1 km^2 window, the spatial accuracy of the active fire product) after the hotspot's date. The overlapping of active fires and FireCCISFD11 showed that 4.2% of the hotspots didn't detect any

Table 2
Estimated accuracy of the MCD64A1 product, in *long* and *short sampling units*. Commission error (CE), omission error (OE), Dice coefficient (DC) and relative bias (relB) are expressed in percentages.

	Commission error (CE)	Omission error (OE)	Dice coefficient (DC)	Relative bias (relB)
Long sampling unit	20.4	59.6	53.6	−49.2
Short sampling unit	33.6	66.3	44.7	−49.2

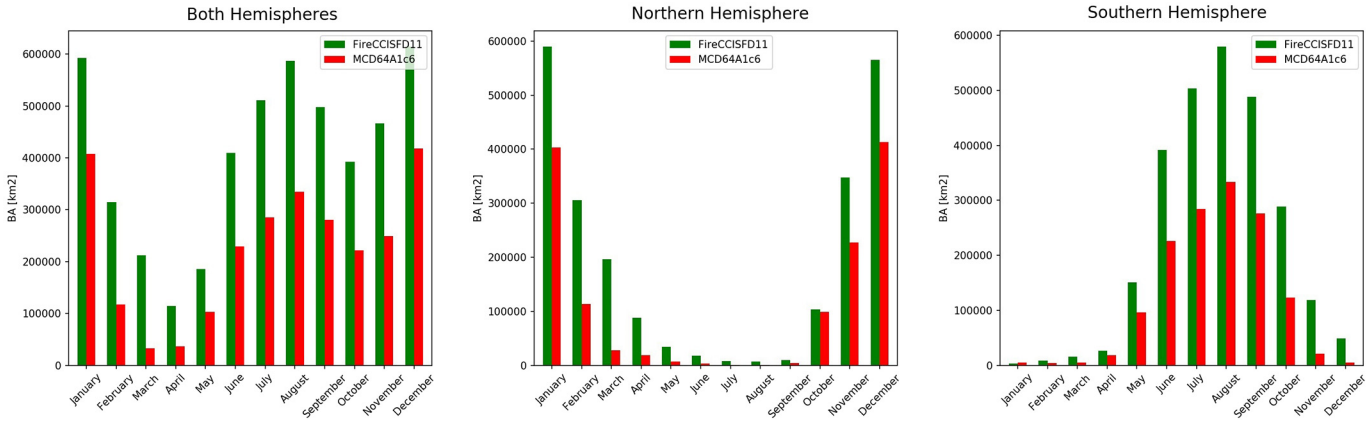

Fig. 9. Distribution of burned areas by month in both FireCCISFD11 and MCD64A1 products, depending on the hemisphere.

burned area around them in the FireCCISFD11, while this percentage was significantly higher for MCD64A1 (49.3%). Fig. 14 shows the histogram of the detection delay for both products. For the FireCCISFD11, the 75.5% of the hotspots were detected in the first available image (no > 10 days after the hotspot's date), 88.7% for BA in the second image at the latest (no > 20 days), and almost 95% earlier than the fourth image (no > 40 days). For the MCD64A1 product the detection delay was much lower as due to the higher temporal resolution (1 day), 68.7% of the hotspots were detected within the first acquisition after the fire (no > 1 day), 76.0% in the second image (no > 2 days), and 80.0% in the fourth image (no > 4 days).

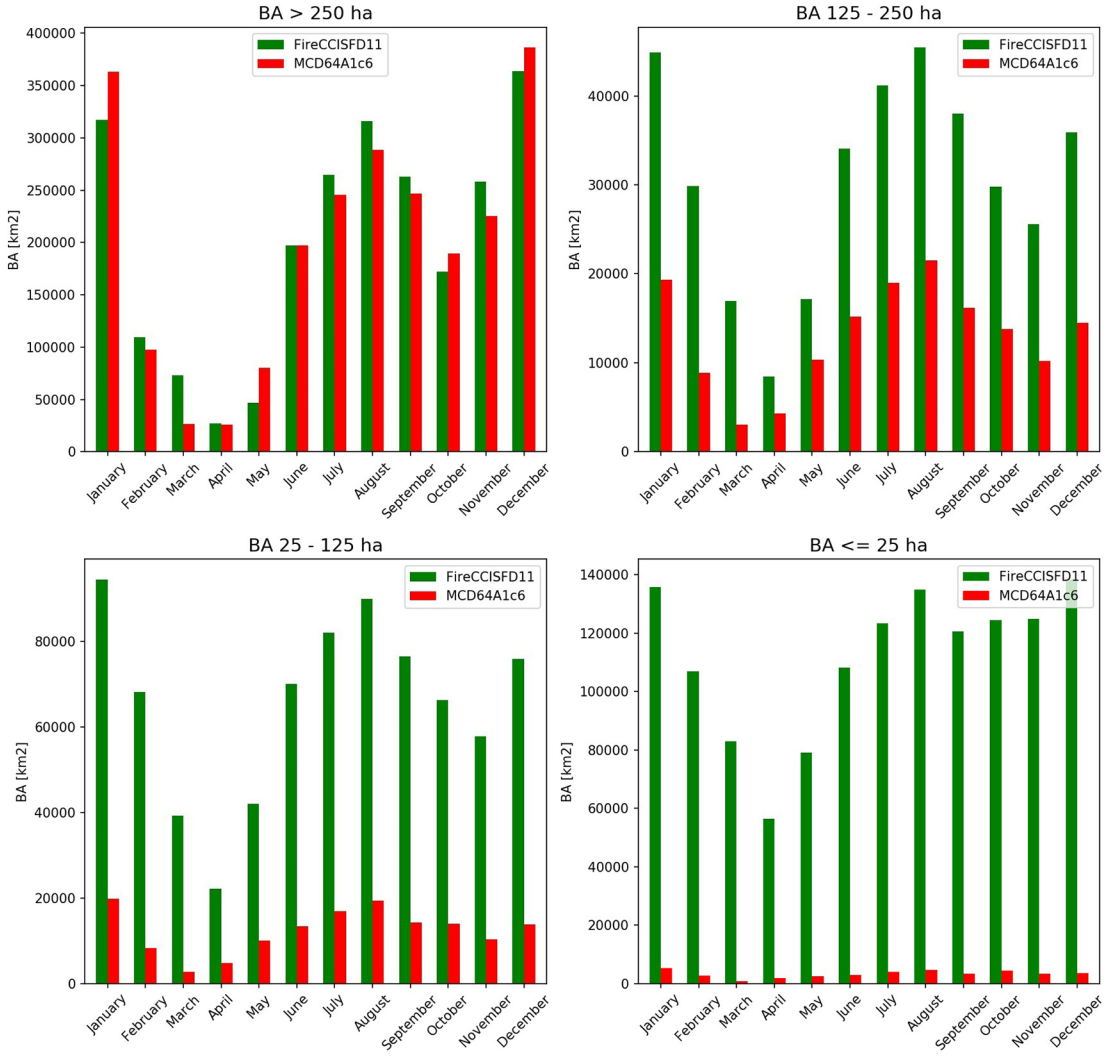

Fig. 10. Distribution of burned area detected in FireCCISFD11 and MCD64A1 grouped by month and patch size.

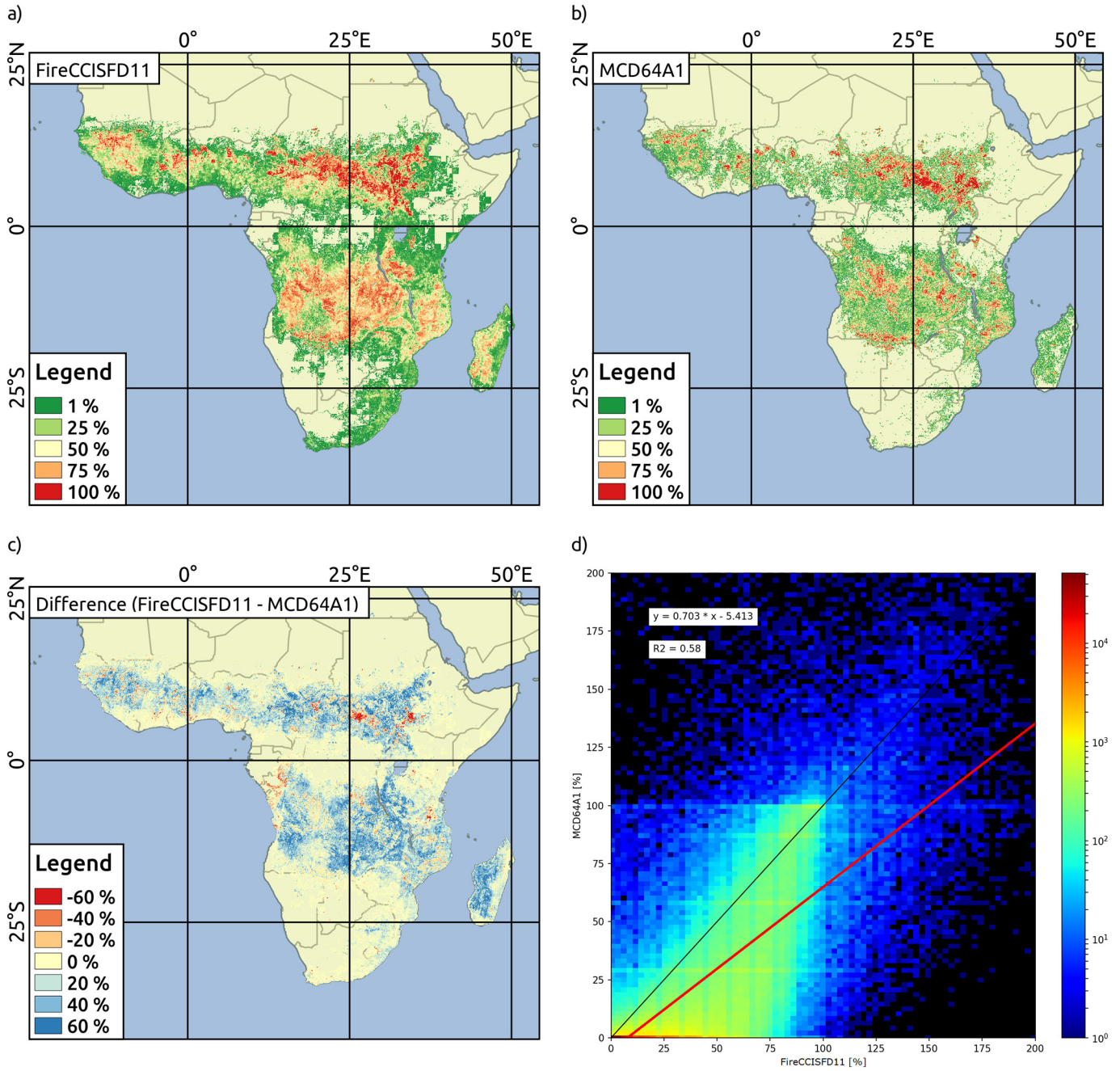

Fig. 11. Aggregated result for the a) FireCCISFD11 and b) MCD64A1 burned areas, representing the fraction of burned surface in a 0.05° grid cell; c) differences between both products, and d) scatter plot and linear regression fitted for the relation between the FireCCISFD11 and MCD64A1 products.

Table 3
Linear regression analysis surface fractions depending on the patch size between FireCCISFD11 and MCD64A1 products.

	Slope	Intercept (%)	R^2
≤25 ha	0.015	0.178	0.036
25–125 ha	0.092	0.719	0.072
125–250 ha	0.023	2.343	0.001
> 250 ha	0.835	4.657	0.571
All sizes	0.703	−5.413	0.580

4. Discussion

This paper presents an algorithm to detect burned areas based on Sentinel-2 MSI images and the MCD14ML MODIS active fires product. The algorithm was implemented operationally and used to generate a new BA product (named FireCCISFD11) that covers the Sub-Saharan Africa for the whole 2016 year, a vast extent of approximately 25 M km^2 covering various biomes (tropical forest, tropical and subtropical savanna, temperate grassland and savanna, and Mediterranean forest, according to Olson et al., 2001). This product involved processing 11 K MSI images in a computation exercise that lasted approximately 6 months.

Even though previous papers have been published using medium resolution data for mapping BA in large regions (such as Hawbaker et al., 2017 and Boschetti et al., 2015 in the US, or Goodwin and Collett, 2014 in Queensland, Australia) this is the first BA continental product generated from medium resolution sensors (in this case Sentinel-2 data) covering a single year. The algorithms by Hawbaker et al., 2017 and Goodwin and Collett, 2014 have some similarities; all of them employ a

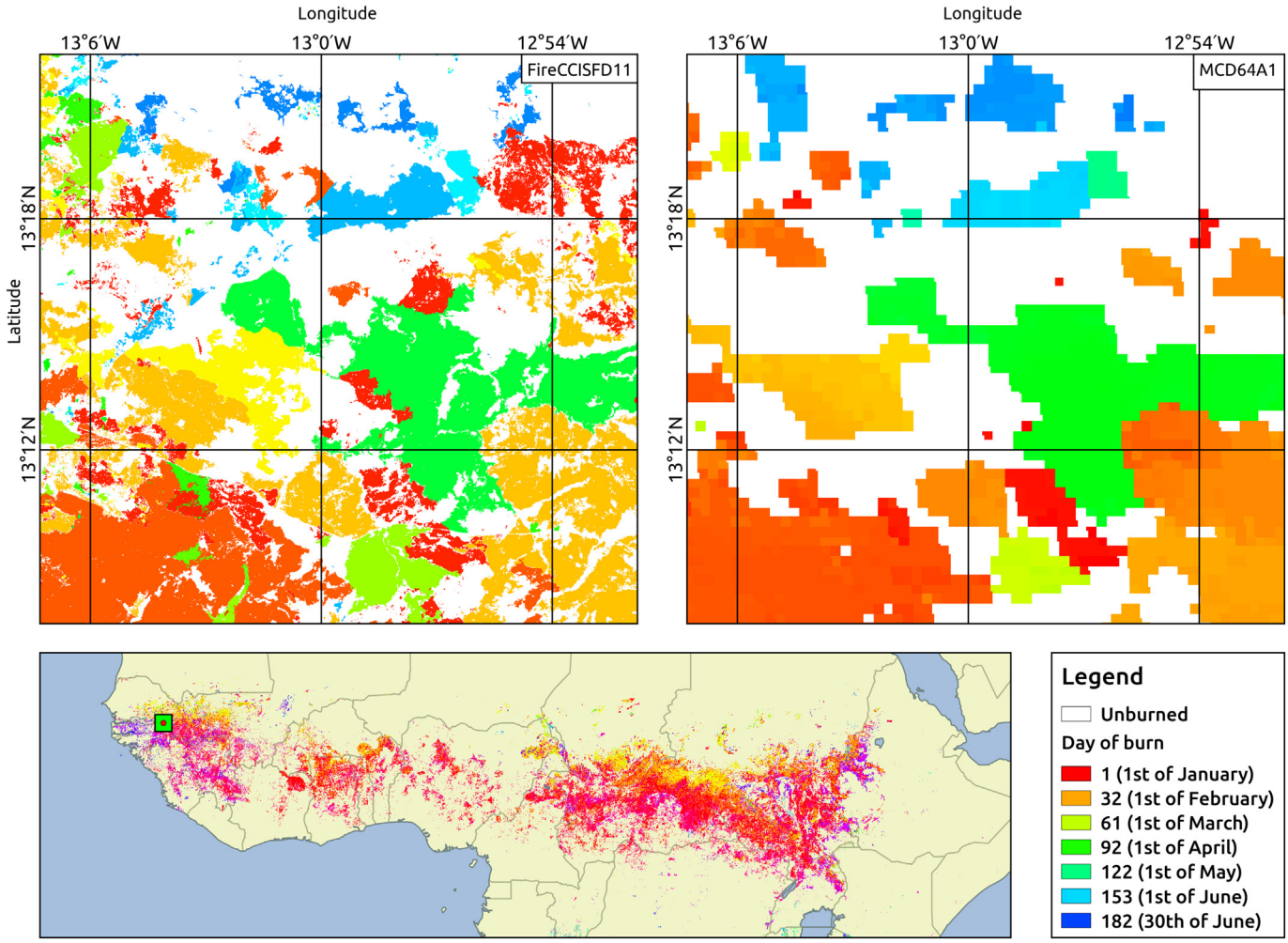

Fig. 12. Sample area of inter-comparison between FireCCISFD11 (left) and MCD64A1 (right) products, located in southeast Senegal.

supervised machine-learning approach based on single or multiple decision trees, adjusted to sample burned data extracted mainly from Landsat images. Both use lagged summaries of Landsat data as a reference against which to measure change, in addition to a region-growing algorithm, although the former used longer lags and also incorporated a wider range of spectral indices as predictors.

The algorithm presented here is more straightforward in this respect: it relies on two very well-known spectral indices—NBR2 and MIRBI- and the NIR spectral region, in a two-phase strategy dependent on MODIS derived active fires. Exploiting the synergy of thermal anomalies detected at the satellite pass and the longer-lasting burned spectral signal is not new (charcoal/ash deposition and removing/alteration of the vegetation) and is the most common strategy used in mapping BA throughout extensive areas globally (Chuvieco et al., 2018; Giglio et al., 2009) as well as continental and regionally (Chen et al., 2017; Merino-De-Miguel et al., 2011; Pereira et al., 2017); however, it has barely been used at a regional/continental scale with higher spatial resolution data (Boschetti et al., 2015). The VIIRS Active fire product was not available at the time the algorithm was designed, but its inclusion can be worthwhile in the future, as it has better spatial resolution than the MODIS product and is likely to provide a greater response over fires of relatively small areas patches (Schroeder et al., 2014, 2008).

A crucial difference of the approach followed here is that after the initialization with fixed thresholds, cut-off values are depending on the individual tile of $100 \times 100\,km^2$ observed between the burned and unburned categories in each of the six predictive variables (posterior and multitemporal difference MIRBI, NBR2, and NIR). Consequently, the approach should be more adaptable to the local conditions than the data-mining models grouped by ecosystems (Hawbaker et al., 2017). However, this tile-based focus produces sometimes a grid effect where some tiles showed significantly more burned area detection than their neighbours, or the other way around. This effect is sometimes more pronounced because the criteria that must have at least one hotspot among the pre-fire and post-fire for being processed, resulting in unprocessed tile gaps.

The algorithm mainly relied on two spectral indices (MIRBI, NBR2) as well as the NIR reflectance, with the latter only being used at the seeding process. Although MIRBI and NBR2 were computed from the same two SWIR bands (B11 and B12 on the case of MSI) they have shown to be complementary due to the different frequency distribution that helps reducing the commission errors working together.

The accuracy estimated for the FireCCISFD11 product was quite encouraging, with much lower omission error and commission errors than global products. These errors increase up to 60% for both errors when short periods of time are considered, which reflects the effects of the date discordance between Landsat and Sentinel acquisitions and the low temporal resolution of Sentinel-2 acquisitions. Errors were found similar to those obtained from other authors using medium resolution sensors with relatively small study regions (Bastarrika et al., 2011; Goodwin and Collett, 2014; Mallinis and Koutsias, 2012; Vanderhoof et al., 2017).

Commission errors detected in the FireCCISFD11 are mainly related to an inaccurate masking of clouds, cloud shadows and terrain shadows

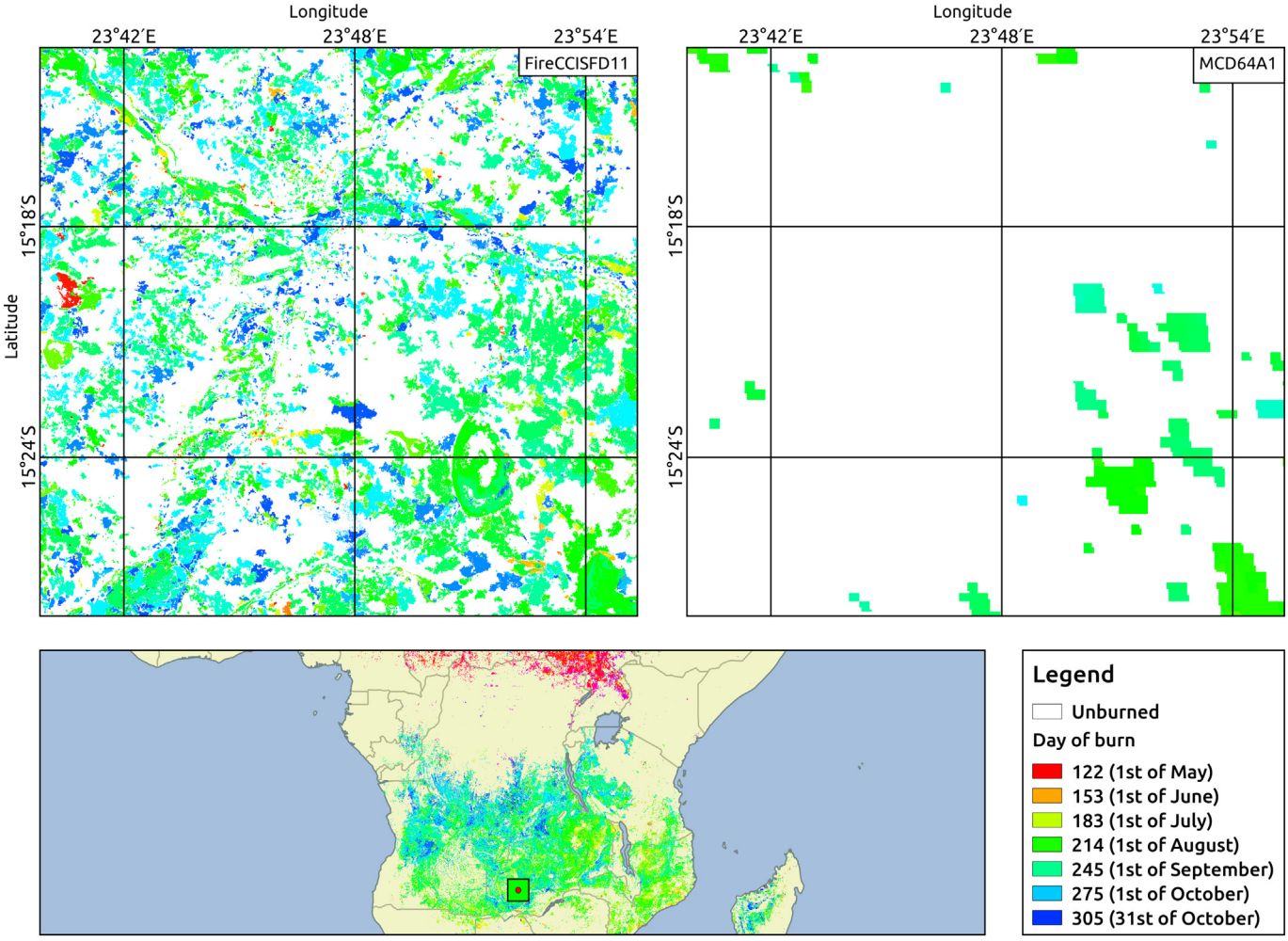

Fig. 13. Sample area of inter-comparison between FireCCISFD11 (left) and MCD64A1 (right) products, located in Zambia.

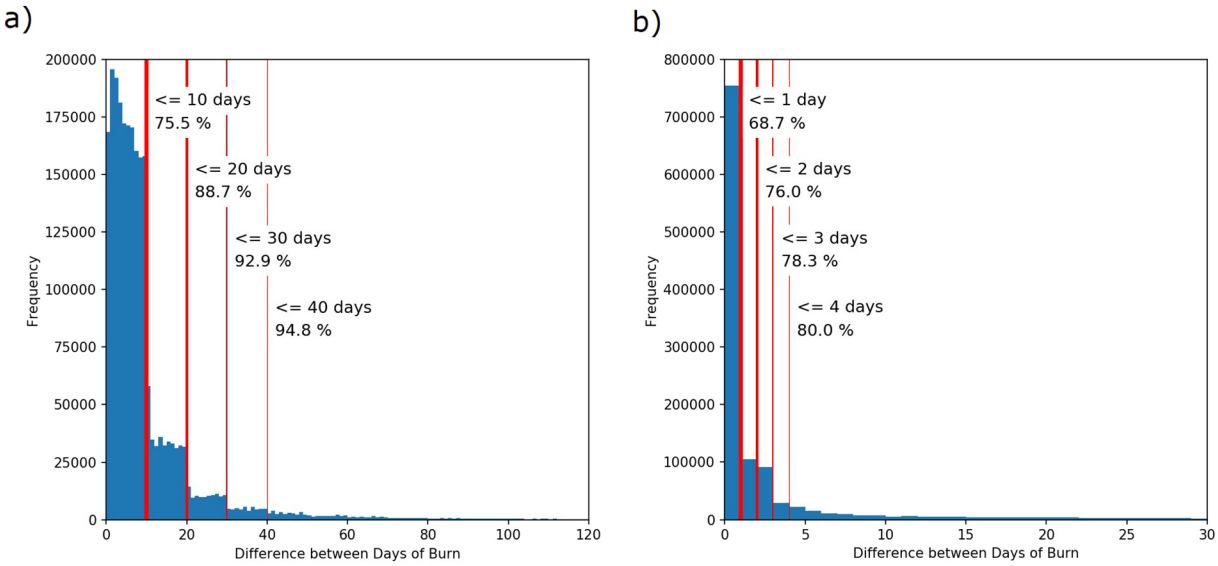

Fig. 14. Detection delay of the a) FireCCISFD11 and b) MCD64A1 comparing to MCD14ML hotspots acquisition date.

that allow locating burned seeds especially in areas where the acquired signal is a mixture of the land surface. The second stage tends to worsen the detection, obtaining many small size burned patches, usually below 25 ha range. The Scene Classification Layer (SCL) derived from the pre-processing stage, when Level-1C product is converted to Level-2A data, has shown to be complex when using to mask the scenes: *cloud shadows* and *low probability clouds* categories detects many burned areas so they are not used in the mask, while several clouds are still observed in the

masked images, even applying a dilation process to *high probability clouds* and *medium probability cloud* and *thin cirrus* categories. The newer sen2cor version 2.2.1 did not improve either this critical situation. An empirical criterion based on Long SWIR (B12) masked quite efficiently the shadows, but a delay in the detection date of very recently burned areas was observed -especially in the savanna biome- that showed very low Long SWIR reflectance values (these areas are mapped at posterior acquisitions when the burned signal is weaker and high enough to fail the shadow criterion). Another commission source observed, also common in BA algorithms previously published (Bastarrika et al., 2011; Hawbaker et al., 2017; Long et al., 2018) are croplands, whose reflectance changes are often indistinguishable from burning, especially in periods where these changes are coincident with fires (during the harvest, postharvest or preplanting periods) (Korontzi et al., 2006). Omission errors are higher than commission and they are mainly related to burned areas with low contrast with the unburned background, due to low severity fires or the gap of time between the fire and the acquisition where charcoal is removed and vegetation starts recovering. In such situations, the contrast between burned and unburned background is not high enough and omissions happen since the initialization step, and therefore the second stage criteria, consider many burned areas as background making their detection unfeasible.

The comparison analysis between the FireCCISFD11 (20 m spatial resolution) with the widely used MCD64A1 collection 6 (based on 500 m spatial resolution MODIS data) emphasised the importance of the input source spatial resolution to map burned areas accurately. MCD64A1, in the same validation dataset as that used for FireCCISFD11, showed an omission error of approximately 60% for the *long sampling unit*, 30% more than the FireCCISFD11. So the FireCCISFD11 is more accurate in *long sampling units* due to its higher spatial resolution, even if the MCD64A1 product is more accurate for *short sampling units*, because of its higher temporal resolution allows the day of detection to be very close to the day of burn. These omissions are produced mainly in burned patches smaller than 250 ha, showing the higher correlation among products for the larger patches, while commission errors for both products were similar, around 20%. The lower temporal resolution of Sentinel-2 data was reflected in detection date accuracy of the products, with approximately 75% of the burned areas were detected in the first acquisition after the fire (10 days), while in the second acquisition (2 days) for the MCD64A1. This better temporal accuracy of the fire date was also noted on the *short sampling unit* validation with only the 34% of commission error for MCD64A1 but up to 64% for the FireCCISFD11. The future use of both Sentinels 2 (A and B) or the combined use of Sentinel-2 and Landsat-8 images may greatly increase this temporal reporting accuracy for medium resolution sensor BA products.

For the whole study area and period (January–December 2016), FireCCISFD11 detected about 80% more BA than MCD64A1, which underlines the relevance of underestimation of small fires in current global products. This numbers must be qualified in the context of the results obtained in the assessment of the products: commission errors in the FireCCISFD11 are related to clouds/shadows that may impact in a false higher burned detection in cloudy areas that have not been fully validated, while commission errors of MCD64A1 are not common and mainly related to the spatial resolution (Giglio et al., 2018, 2009). The presence of commissions in cloud edges points to the significance of refining clouds masks. Moreover, the validation sites were selected proportionally to the BA in the MCD64A1 product (Section 2.5), so areas where only small fires occur (with low burned area in MCD64A1) may have been missed in the assessment process.

The BA mapping at medium spatial resolution of FireCCISFD11 is crucial to improve the accuracy of the emission of greenhouse gases into the atmosphere, and for many other applications as land management, environmental, climate change adaptation and land cover change applications.

5. Conclusions

An automatic BA mapping algorithm based on Sentinel-2 MSI data is presented in this paper, in order to emphasize the importance of the spatial resolution of this sensor in mapping accurately small burned areas. The FireCCISFD11 product in Sub-Saharan Africa generated by this algorithm is an innovation, since there were very few BA products at high spatial resolution (30 m from Landsat data at best) covering such a large area until now, and none derived from S2 MSI imagery (at 20 m spatial resolution).

The assessment using Landsat data shows that both commissions and omissions are much lower than those measured for global BA products, due to the ability of the FireCCISFD11 to detect small fires that were at a sub-pixel scale in other products. The FireCCISFD11 detects 80% more BA than the global MCD64A1 product in 2016, most of them being burned patches smaller than 250 ha, which signals how much the total BA may have been underestimated in global products. However, the FireCCISFD11 is not so accurate temporally, since the long revisit period of the S2 satellite (10 days) and the presence of clouds delay the detection date; the revisit period will be shorter in the future if a product with S2 data from April 2017 onwards is produced, when both S2-A and S2-B satellites are in orbit with a 5-day revisit.

The next step for the product is to apply the algorithm at a global scale with necessary changes, especially improving the clouds and cloud shadows detection, which is now the main source of commission errors. We also think the product would improve if MODIS hotspots from the MCD14ML were replaced by VIIRS hotspots, which have a better spatial resolution but were not available yet when we designed this algorithm. Creating a global BA product at 20 m would certainly increase the amount of the total burned area. Its implications in different applications (greenhouse gas emissions, land cover changes, land management, etc.) should be analysed in due time.

Acknowledgments

This research was carried out within the Fire_cci project (https://www.esa-fire-cci.org/, last accessed on November 2018), contract no. 4000115006/15/I-NB, which has been funded by the European Space Agency (ESA) under the Climate Change Initiative Programme. The FireCCISFD11 product can be downloaded at https://www.esa-fire-cci.org/node/262 (last accessed on November 2018).

References

Alonso-Canas, I., Chuvieco, E., 2015. Global burned area mapping from ENVISAT-MERIS and MODIS active fire data. Remote Sens. Environ. 163, 140–152. https://doi.org/10.1016/j.rse.2015.03.011.

Andreae, M.O., Metlet, P., 2001. Emission of trace gases and aerosols from biomass burning. Glob. Biogeochem. Cycles 15, 955–966.

Bastarrika, A., Chuvieco, E., Martín, M.P., 2011. Mapping burned areas from Landsat TM/ETM+ data with a two-phase algorithm: balancing omission and commission errors. Remote Sens. Environ. 115, 1003–1012. https://doi.org/10.1016/j.rse.2010.12.005.

Bastarrika, A., Alvarado, M., Artano, K., Martinez, M., Mesanza, A., Torre, L., Ramo, R., Chuvieco, E., 2014. BAMS: a tool for supervised burned area mapping using Landsat data. Remote Sens. 6, 12360–12380. https://doi.org/10.3390/rs61212360.

Boschetti, L., Roy, D., Justice, C., 2009. International global burned area satellite product validation protocol. In: Cal Val, C. (Ed.), Part I - Production and Standardization of Validation Reference Data. Committee on Earth Observation Satellites, USA, pp. 1–11.

Boschetti, L., Roy, D.P., Justice, C.O., Humber, M.L., 2015. MODIS–Landsat fusion for large area 30 m burned area mapping. Remote Sens. Environ. 161, 27–42. https://doi.org/10.1016/j.rse.2015.01.022.

Bowman, D.M.J.S., Balch, J.K., Artaxo, P., Bond, W.J., Carlson, J.M., Cochrane, M.A., D'Antonio, C.M., DeFries, R.S., Doyle, J.C., Harrison, S.P., Johnston, F.H., Keeley, J.E., Krawchuk, M.A., Kull, C.A., Marston, J.B., Moritz, M.A., Prentice, I.C., Roos, C.I., Scott, A.C., Swetnam, T.W., van der Werf, G.R., Pyne, S.J., 2009. Fire in the earth system. Science 324, 481–484.

Chen, D., Pereira, J.M.C., Masiero, A., Pirotti, F., 2017. Mapping fire regimes in China using MODIS active fire and burned area data. Appl. Geogr. 85, 14–26. https://doi.org/10.1016/J.APGEOG.2017.05.013.

Chuvieco, E., Martín, M.P., Palacios, A., 2002. Assessment of different spectral indices in the red-near-infrared spectral domain for burned land discrimination. Int. J. Remote

Sens. 23, 5103–5110. https://doi.org/10.1080/01431160210153129.
Chuvieco, E., Yue, C., Heil, A., Mouillot, F., Alonso-Canas, I., Padilla, M., Pereira, J.M., Oom, D., Tansey, K., 2016. A new global burned area product for climate assessment of fire impacts. Glob. Ecol. Biogeogr. 25, 619–629. https://doi.org/10.1111/geb.12440.
Chuvieco, E., Lizundia-Loiola, J., Pettinari, M.L., Ramo, R., Padilla, M., Tansey, K., Mouillot, F., Laurent, P., Storm, T., Heil, A., Plummer, S., 2018. Generation and analysis of a new global burned area product based on MODIS 250 m reflectance bands and thermal anomalies. Earth Syst. Sci. Data Discuss. 1–24. https://doi.org/10.5194/essd-2018-46.
Dice, L.R., 1945. Measures of the amount of ecologic association between species. Ecology 26, 297–302. https://doi.org/10.2307/1932409.
Drusch, M., Del Bello, U., Carlier, S., Colin, O., Fernandez, V., Gascon, F., Hoersch, B., Isola, C., Laberinti, P., Martimort, P., Meygret, A., Spoto, F., Sy, O., Marchese, F., Bargellini, P., 2012. Sentinel-2: ESA's optical high-resolution mission for GMES operational services. Remote Sens. Environ. 120, 25–36. https://doi.org/10.1016/j.rse.2011.11.026.
ESA, 2011. MSI Instrument – Sentinel-2 MSI Technical Guide – Sentinel Online [WWW Document].
Fleiss, J.L., 1981. Statistical Methods for Rates and Proportions. Wiley.
Fraser, R.H., Li, Z., Cihlar, J., 2000. Hotspot and NDVI differencing synergy (HANDS): a new technique for burned area mapping over boreal forest. Remote Sens. Environ. 74, 362–376. https://doi.org/10.1016/S0034-4257(00)00078-X.
Fraser, R.H., Fernandes, R., Latifovic, R., 2002. Multi-temporal burned area mapping using logistic regression analysis and change metrics. In: IEEE International Geoscience and Remote Sensing Symposium, pp. 1486–1488. https://doi.org/10.1109/IGARSS.2002.1026157.
García, M.J.L., Caselles, V., 1991. Mapping burns and natural reforestation using thematic Mapper data. Geocarto Int. 6, 31–37. https://doi.org/10.1080/10106049109354290.
Giglio, L., Csiszar, I., Justice, C.O., 2006a. Global distribution and seasonality of active fires as observed with the Terra and Aqua Moderate Resolution Imaging Spectroradiometer (MODIS) sensors. J. Geophys. Res. Biogeosci. 111https://doi.org/10.1029/2005JG000142. (n/a-n/a).
Giglio, L., van der Werf, G.R., Randerson, J.T., Collatz, G.J., Kasibhatla, P., 2006b. Global estimation of burned area using MODIS active fire observations. Atmos. Chem. Phys. 6, 957–974. https://doi.org/10.5194/acp-6-957-2006.
Giglio, L., Loboda, T., Roy, D.P., Quayle, B., Justice, C.O., 2009. An active-fire based burned area mapping algorithm for the MODIS sensor. Remote Sens. Environ. 113, 408–420. https://doi.org/10.1016/j.rse.2008.10.006.
Giglio, L., Randerson, J.T., van der Werf, G.R., Kasibhatla, P.S., Collatz, G.J., Morton, D.C., DeFries, R.S., 2010. Assessing variability and long-term trends in burned area by merging multiple satellite fire products. Biogeosciences 7, 1171–1186. https://doi.org/10.5194/bg-7-1171-2010.
Giglio, L., Randerson, J.T., van der Werf, G.R., 2013. Analysis of daily, monthly, and annual burned area using the fourth-generation global fire emissions database (GFED4). J. Geophys. Res. Biogeosci. 118, 317–328. https://doi.org/10.1002/jgrg.20042.
Giglio, L., Schroeder, W., Justice, C.O., 2016. The collection 6 MODIS active fire detection algorithm and fire products. Remote Sens. Environ. 178, 31–41. https://doi.org/10.1016/j.rse.2016.02.054.
Giglio, L., Boschetti, L., Roy, D.P., Humber, M.L., Justice, C.O., 2018. The collection 6 MODIS burned area mapping algorithm and product. Remote Sens. Environ. 217, 72–85. https://doi.org/10.1016/j.rse.2018.08.005.
Gómez, C., White, J.C., Wulder, M.A., 2016. Optical remotely sensed time series data for land cover classification: a review. ISPRS J. Photogramm. Remote Sens. https://doi.org/10.1016/j.isprsjprs.2016.03.008.
Goodwin, N.R., Collett, L.J., 2014. Development of an automated method for mapping fire history captured in Landsat TM and ETM+ time series across Queensland, Australia. Remote Sens. Environ. 148, 206–221. https://doi.org/10.1016/j.rse.2014.03.021.
Grégoire, J.M., Eva, H.D., Belward, A.S., Palumbo, I., Simonetti, D., Brink, A., 2013. Effect of land-cover change on Africa's burnt area. Int. J. Wildland Fire 22, 107–120. https://doi.org/10.1071/WF11142.
Hantson, S., Padilla, M., Corti, D., Chuvieco, E., 2013. Strengths and weaknesses of MODIS hotspots to characterize global fire occurrence. Remote Sens. Environ. 131, 152–159. https://doi.org/10.1016/j.rse.2012.12.004.
Hantson, S., Lasslop, G., Kloster, S., Chuvieco, E., 2015. Anthropogenic effects on global mean fire size. Int. J. Wildland Fire 24, 589–596. https://doi.org/10.1071/WF14208.
Hawbaker, T.J., Vanderhoof, M.K., Beal, Y.-J., Takacs, J.D., Schmidt, G.L., Falgout, J.T., Williams, B., Fairaux, N.M., Caldwell, M.K., Picotte, J.J., Howard, S.M., Stitt, S., Dwyer, J.L., 2017. Mapping burned areas using dense time-series of Landsat data. Remote Sens. Environ. 198, 504–522. https://doi.org/10.1016/j.rse.2017.06.027.
Huang, H., Roy, D.P., Boschetti, L., Zhang, H.K., Yan, L., Kumar, S.S., Gomez-Dans, J., Li, J., 2016. Separability analysis of Sentinel-2A Multi-Spectral Instrument (MSI) data for burned area discrimination. Remote Sens. 8. https://doi.org/10.3390/rs8100873.
Huete, A.R., 1988. A soil-adjusted vegetation index (SAVI). Remote Sens. Environ. 25, 295–309. https://doi.org/10.1016/0034-4257(88)90106-X.
Huete, A.R., Justice, C., Liu, H., 1994. Development of vegetation and soil indexes for Modis-EOS. Remote Sens. Environ. 49, 224–234. https://doi.org/10.1016/0034-4257(94)90018-3.
Kaufman, Y.J., Remer, L.A., 1994. Detection of forests using mid-IR reflectance: an application for aerosol studies. IEEE Trans. Geosci. Remote Sens. 32, 672–683. https://doi.org/10.1109/36.297984.
Key, C.H., Benson, N., 1999. The Normalized Burn Ratio (NBR): A Landsat TM Radiometric Measure of Burn Severity. US Geol. Surv. North. Rocky Mt. Sci. Center.
Korontzi, S., McCarty, J., Loboda, T., Kumar, S., Justice, C., 2006. Global distribution of agricultural fires in croplands from 3 years of Moderate Resolution Imaging Spectroradiometer (MODIS) data. Glob. Biogeochem. Cycles 20. https://doi.org/10.1029/2005GB002529.
Koutsias, N., Karteris, M., 2000. Burned area mapping using logistic regression modeling of a single post-fire Landsat-5 Thematic Mapper image. Int. J. Remote Sens. 21, 673–687. https://doi.org/10.1080/014311600210506.
Lasaponara, R., 2006. Estimating spectral separability of satellite derived parameters for burned areas mapping in the Calabria region by using SPOT-Vegetation data. Ecol. Model. 196, 265–270. https://doi.org/10.1016/j.ecolmodel.2006.02.025.
Lewis, S.L., Edwards, D.P., Galbraith, D., 2015. Increasing human dominance of tropical forests. Science. https://doi.org/10.1126/science.aaa9932.
Long, T., Zhang, Z., He, G., Jiao, W., Tang, C., Wu, B., Zhang, X., Wang, G., Yin, R., 2018. 30 m Resolution Global Annual Burned Area Mapping Based on Landsat Images and Google Earth Engine.
Mallinis, G., Koutsias, N., 2012. Comparing ten classification methods for burned area mapping in a Mediterranean environment using Landsat TM satellite data. Int. J. Remote Sens. 33, 4408–4433. https://doi.org/10.1080/01431161.2011.648284.
Martín, M.P., Chuvieco, E., 1998. Cartografía de grandes insendios forestales en la península Ibérica a partir de imágenes NOAA-AVHRR. In: Teledetección Av. y Apl, pp. 248–251.
Martin, P., Gómez, I., Chuvieco, E., 2005. Performance of a burned-area index (BAIM) for mapping Mediterranean burned scars from MODIS data. In: Proceedings of the 5th International Workshop on Remote Sensing and GIS Application to Forest Fire Management: Fire Effects Assessment, pp. 193–197.
Merino-De-Miguel, S., González-Alonso, F., Huesca, M., Armenteras, D., Franco, C., Topografía, U., 2011. MODIS reflectance and active fire data for burn mapping in Colombia. Earth Interact. 15. https://doi.org/10.1175/2010EI344.1.
Olson, D.M., Dinerstein, E., Wikramanayake, E.D., Burgess, N.D., Powell, G.V.N., Underwood, E.C., D'amico, J.A., Itoua, I., Strand, H.E., Morrison, J.C., Loucks, C.J., Allnutt, T.F., Ricketts, T.H., Kura, Y., Lamoreux, J.F., Wettengel, W.W., Hedao, P., Kassem, K.R., 2001. Terrestrial ecoregions of the world: a new map of life on earth. Bioscience 51, 933. https://doi.org/10.1641/0006-3568(2001)051[0933:TEOTWA]2.0.CO;2.
Padilla, M., Stehman, S.V., Litago, J., Chuvieco, E., 2014. Assessing the temporal stability of the accuracy of a time series of burned area products. Remote Sens. 6, 2050–2068. https://doi.org/10.1207/s15327752jpa4405_22.
Padilla, M., Stehman, S.V., Ramo, R., Corti, D., Hantson, S., Oliva, P., Alonso-Canas, I., Bradley, A.V., Tansey, K., Mota, B., Pereira, J.M., Chuvieco, E., 2015. Comparing the accuracies of remote sensing global burned area products using stratified random sampling and estimation. Remote Sens. Environ. 160, 114–121. https://doi.org/10.1016/j.rse.2015.01.005.
Pereira, J.M.C., Sa, A.C.L., Sousa, A.M.O., Silva, J.M.N., Santos, M.T.N., JMBC, 1999. Spectral characterisation and discrimination of burnt areas. In: Chuvieco, E. (Ed.), Remote Sensing of Large Wildfires in the European Mediterranean Basin, pp. 123–138.
Pereira, A.A., Pereira, J.M.C., Libonati, R., Oom, D., Setzer, A.W., Morelli, F., Machado-Silva, F., de Carvalho, L.M.T., 2017. Burned area mapping in the Brazilian Savanna using a one-class support vector machine trained by active fires. Remote Sens. 9. https://doi.org/10.3390/rs9111161.
Pinty, B., Verstraete, M.M., 1992. GEMI: a non-linear index to monitor global vegetation from satellites. Vegetatio 101, 15–20. https://doi.org/10.1007/BF00031911.
Plummer, S., Arino, O., Simon, M., Steffen, W., 2006. Establishing a earth observation product service for the terrestrial carbon community: the GLOBCARBON Initiative. Mitig. Adapt. Strateg. Glob. Chang. 11, 97–111. https://doi.org/10.1007/s11027-006-1012-8.
Pu, R., Gong, P., 2004. Determination of burnt scars using logistic regression and neural network techniques from a single post-fire Landsat 7 ETM+ image. Photogramm. Eng. Remote. Sens. 70, 841–850. https://doi.org/10.14358/PERS.70.7.841.
Randerson, J.T., Chen, Y., van der Werf, G.R., Rogers, B.M., Morton, D.C., 2012. Global burned area and biomass burning emissions from small fires. J. Geophys. Res. Biogeosci. 117https://doi.org/10.1029/2012JG002128. (n/a-n/a).
Rouse, J.W., Haas, R.H., Schell, J.A., 1974. Monitoring the Vernal Advancement and Retrogradation (Greenwave Effect) of Natural Vegetation. NASA Goddard Sp. Flight Cent (doi:19740008955).
Roy, D.P., Boschetti, L., Justice, C.O., Ju, J., 2008. The collection 5 MODIS burned area product — global evaluation by comparison with the MODIS active fire product. Remote Sens. Environ. 112, 3690–3707. https://doi.org/10.1016/j.rse.2008.05.013.
Schroeder, W., Prins, E., Giglio, L., Csiszar, I., Schmidt, C., Morisette, J., Morton, D., 2008. Validation of GOES and MODIS active fire detection products using ASTER and ETM + data. Remote Sens. Environ. 112, 2711–2726. https://doi.org/10.1016/j.rse.2008.01.005.
Schroeder, W., Oliva, P., Giglio, L., Csiszar, I.A., 2014. The New VIIRS 375 m active fire detection data product: algorithm description and initial assessment. Remote Sens. Environ. 143, 85–96. https://doi.org/10.1016/j.rse.2013.12.008.
Schroeder, W., Oliva, P., Giglio, L., Quayle, B., Lorenz, E., Morelli, F., 2016. Active fire detection using Landsat-8/OLI data. Remote Sens. Environ. 185, 210–220. https://doi.org/10.1016/j.rse.2015.08.032.
Simon, M., Plummer, S., Fierens, F., Hoelzemann, J.J., Arino, O., 2004. Burnt area detection at global scale using ATSR-2: the GLOBSCAR products and their qualification. J. Geophys. Res. 109, D14S02. https://doi.org/10.1029/2003JD003622.
Smith, A.M.S., Drake, N.A., Wooster, M.J., Hudak, A.T., Holden, Z.A., Gibbons, C.J., 2007. Production of Landsat ETM+ reference imagery of burned areas within Southern African savannahs: comparison of methods and application to MODIS. Int. J. Remote Sens. 28, 2753–2775. https://doi.org/10.1080/01431160600954704.
Stroppiana, D., Bordogna, G., Carrara, P., Boschetti, M., Boschetti, L., Brivio, P.A., 2012. A method for extracting burned areas from Landsat TM/ETM+ images by soft

aggregation of multiple Spectral Indices and a region growing algorithm. ISPRS J. Photogramm. Remote Sens. 69, 88–102. https://doi.org/10.1016/j.isprsjprs.2012.03.001.

Stroppiana, D., Azar, R., Calò, F., Pepe, A., Imperatore, P., Boschetti, M., Silva, J., Brivio, P., Lanari, R., 2015. Received: 4 May 2014/Accepted: 12 January 2015/Published: 26 January 2015. Remote Sens. 7, 1320–1345. https://doi.org/10.3390/rs70201320.

Tansey, K., Grégoire, J., Stroppiana, D., Sousa, A., Silva, J., Pereira, J.M.C., Boschetti, L., Maggi, M., Brivio, P.A., Fraser, R., Flasse, S., Ershov, D., Binaghi, E., Graetz, D., Peduzzi, P., 2004. Vegetation burning in the year 2000: global burned area estimates from SPOT VEGETATION data. J. Geophys. Res. 109, D14S03. https://doi.org/10.1029/2003JD003598.

Tansey, K., Beston, J., Hoscilo, A., Page, S.E., Paredes Hernández, C.U., 2008. Relationship between MODIS fire hot spot count and burned area in a degraded tropical peat swamp forest in Central Kalimantan, Indonesia. J. Geophys. Res. 113, D23112. https://doi.org/10.1029/2008JD010717.

Trigg, S., Flasse, S., 2001. An evaluation of different bi-spectral spaces for discriminating burned shrub-savannah. Int. J. Remote Sens. 22, 2641–2647. https://doi.org/10.1080/01431160110053185.

Van Der Werf, G.R., Randerson, J.T., Giglio, L., Van Leeuwen, T.T., Chen, Y., Rogers, B.M., Mu, M., Van Marle, M.J.E., Morton, D.C., Collatz, G.J., Yokelson, R.J., Kasibhatla, P.S., 2017. Global fire emissions estimates during 1997–2016. Earth Syst. Sci. Data. https://doi.org/10.5194/essd-9-697-2017.

Vanderhoof, M.K., Fairaux, N., Beal, Y.-J.G., Hawbaker, T.J., 2017. Validation of the USGS Landsat Burned Area Essential Climate Variable (BAECV) across the conterminous United States. Remote Sens. Environ. 198, 393–406. https://doi.org/10.1016/j.rse.2017.06.025.

Veraverbeke, S., Harris, S., Hook, S., 2011. Evaluating spectral indices for burned area discrimination using MODIS/ASTER (MASTER) airborne simulator data. Remote Sens. Environ. 115, 2702–2709. https://doi.org/10.1016/j.rse.2011.06.010.